
Volume 45, June 2013
ISSN 0749-6419
ELSEVIER
INTERNATIONAL JOURNAL OF
Plasticity
Editor-in-Chief
Akhtar S. Khan,
University of Maryland–Baltimore County
Special Issue
In Honor of Rob Wagoner
Guest Editors
Jeong Whan Yoon, Swinburne University of Technology
Thomas B. Stoughton, General Motors R&D Center
Available online at www.sciencedirect.com
SciVerse ScienceDirect

International Journal of Plasticity 45 (2013) 140–159

Contents lists available at SciVerse ScienceDirect

International Journal of Plasticity

journal homepage: www.elsevier.com/locate/ijplas

Extension of quasi-plastic–elastic approach to incorporate complex plastic flow behavior – application to springback of advanced high-strength steels

Jinwoo Lee [a], Jeong-Yeon Lee [a], Frédéric Barlat [a], R.H. Wagoner [b], Kwansoo Chung [c], Myoung-Gyu Lee [a,*]

[a] Graduate Institute of Ferrous Technology (GIFT), Pohang University of Science and Technology (POSTECH), Pohang 790-784, South Korea
[b] Department of Material Science and Engineering, The Ohio State University, Columbus, OH 43210, USA
[c] Department of Materials Science and Engineering, Seoul National University, Seoul 151-742, South Korea

ARTICLE INFO

Article history:
Received 5 June 2012
Received in final revised form 14 November 2012
Available online 8 February 2013

Keywords:
Quasi-plastic–elastic
Anisotropic hardening
Bauschinger effect
Springback
AHSS

ABSTRACT

Materials modeling and numerical formulations were conducted to describe the complex material behavior upon strain path change in order to enhance the prediction accuracy of springback in advanced high strength steels (AHSS). An approach without kinematic hardening rule, or the homogeneous anisotropic hardening (HAH) model, was incorporated to the newly conceived quasi-plastic–elastic strain (QPE) formulations. The HAH model is able to capture complex plastic flow behavior of sheet metals such as the Bauschinger effect, transient behavior, work-hardening stagnation and permanent softening. The QPE approach was developed to reproduce the nonlinear elastic behavior during unloading and reloading. The two models were independently validated for predicting springback, with better performance than conventional constitutive models. In this study, the two models are combined and extended to enhance the prediction capability of springback in AHSS. For this purpose, fully implicit numerical algorithms were re-formulated to link the two modeling approaches using general anisotropic yield function and hardening for shell element. The original model was only valid for continuum isotropic element with analytical stress integration procedure. Simulations of 2D draw bending test were performed to validate the developed approach for two AHSS, DP780 and TRIP780, sheets. The springback prediction was significantly improved if most of the complex material behavior relating to elasticity and plasticity were taken into account in the finite element simulations.

1. Introduction

In sheet metal forming, springback – undesired shape changes due to elastic recovery – is one of the most critical problems to be solved during process optimization. The springback is more pronounced when materials have higher strength and/or lower elastic modulus. For example, among recent emerging materials, advanced high strength steels (AHSS) produce larger springback than conventional mild steels because of their much higher strength, while aluminum and magnesium alloys do because of their lower elastic moduli. For this reason, considerable efforts have been made to predict springback accurately by numerical simulation in the tool design stage. For a better prediction of springback with finite

---

* Corresponding author. Tel.: +82 54 279 9034; fax: +82 54 279 9299.
E-mail address: mglee@postech.ac.kr (M.-G. Lee).

0749-6419/$ - see front matter © 2013 Elsevier Ltd. All rights reserved.
http://dx.doi.org/10.1016/j.ijplas.2013.01.011

element (FE) analysis, two main factors have been investigated. These efforts have addressed the numerical parameters, which include the number of integration points, element type, mesh size and the numerical integration scheme (Li et al., 2002), as well as the constitutive laws used for the simulations. The material modeling has become especially important because newly emerging materials exhibit more complex deformation behavior with loading path changes (Barlat et al., 2011; Chung et al., 2005; Geng et al., 2002; Lee et al., 2007). The complex material response during loading–unloading–reverse loading needs to be considered for accurate simulation of springback, involving the exact modeling of anisotropic plastic hardening (Lee et al., 2011) and nonlinear elastic unloading/reloading response (Sun and Wagoner, 2011; Yoshida et al., 2002).

Sheet materials in typical sheet forming processes experience continuous bending–unbending with superimposed tensile force. Therefore, the material behavior under reverse loading must be known in addition to the usual monotonic uniaxial behavior. A typical stress–strain curve under loading–reverse loading has four main characteristics; (1) The Bauschinger effect (early re-yielding when the load is reversed), (2) transient behavior (rapid hardening in the elastic–plastic transient region towards the forward flow stress curve), (3) work-hardening stagnation (lower or stagnating work hardening rate), and (4) permanent softening (existence of a permanent gap between forward and reversed flow curves) (Yoshida and Uemori, 2002). Because these deformation characteristics cannot be captured by the classical isotropic hardening law, simple linear kinematic hardening models were proposed by Prager (1956) and Ziegler (1959) to represent the Bauschinger effect. A better description of reversed flow stress curve was later proposed by Armstrong and Frederick (1966) introducing a nonlinear kinematic hardening approach with the addition of the so-called dynamic recovery term. Furthermore, Chaboche (1986) improved it to describe ratcheting effects during cyclic loading. Many improved kinematic hardening laws have been implemented into FE simulation for sheet metal forming applications to predict springback or formability (Aretz, 2008; Choi et al., 2006a, b; Chung et al., 2005; Lee et al., 2005a,b, 2007; Oliveira et al., 2007; Yoshida and Uemori, 2002).

With the increasing complexity of material deformation behavior, other approaches not based on fully kinematic hardening behavior have been proposed. The distortional hardening approach combined with the conventional kinematic hardening is an example in this category (Feigenbaum and Dafalias, 2007, 2008; François, 2001; Hill et al., 1994; Kurtyka and Życzkowski, 1996; Vincent et al., 2002; Voyiadjis and Foroozesh, 1990; Wu, 2002). For instance, Wu (2003, 2007) explained the nonlinear distortion and translation of the yield surface using the convected coordinate systems. More recently, without using the kinematic hardening concept, the homogeneous yield function-based anisotropic hardening (HAH) was proposed (Barlat et al., 2011). When a material is subjected to a monotonic deformation, the HAH model describes a plastic deformation as an expansion of the yield locus exactly the same way as the classical isotropic hardening law near the loading direction, but its opposite side is distorted or flattened. In order to describe the effect of strain path change, this model introduces the microstructure deviator variable, which tracks the previous loading history and determines the evolution of the yield surface distortion. Moreover, any isotropic or anisotropic yield function can be incorporated in order to describe the isotropic or anisotropic yielding behavior for orthotropic materials. The HAH model was implemented into the FE software ABAQUS successfully, and used in the simulation of the U-draw bending for AHSS sheets to predict springback (ABAQUS, 2010; Lee et al., 2012a,b). More recently, the HAH model was extended to describe the material behavior on the complex strain path changes such as cross-loading effect (Barlat et al., 2012).

As the strength of automotive steels increases with higher springback, knowledge of the material's elastic behavior becomes essential. This is related to the increase of plastic potential at unloading, which results in more pronounced elastic deformation during unloading. Moreover, recent experimental studies have shown that the elastic deformation during unloading (or reloading) is not perfectly linear but the slope continuously decreases as the unloading (or reloading) proceeds (Andar et al., 2010; Chatti and Hermi, 2011; Cleveland and Ghosh, 2002; Eggertsen and Mattiasson, 2010; Geng and Wagoner, 2002; Morestin and Boivin, 1996; Sun and Wagoner, 2011; Yamaguchi et al., 1998; Yang et al., 2004). One of the practical approaches to incorporate the change of unloading elastic modulus is so-called chord modulus concept. The chord modulus is defined as the slope of a straight line between the stress point before unloading and the zero stress point after unloading. It is also reported that the chord modulus decreases as the plastic pre-strain increases. The chord modulus tends to be saturated at about 20% of the initial Young's modulus after a strain of about 10% for many sheet steels. An advantage of the chord modulus concept is the easy implementation into FE analysis. The simulations with chord modulus approach produced remarkable improvement in springback prediction (Fei and Hodgson, 2006; Yoshida et al., 2002; Yu, 2009; Zang et al., 2007).

Although the chord modulus approach has improved the modeling ability for the nonlinear elastic unloading, there is an issue to be resolved. With this approach, upon springback, the stress does not always completely vanish like it is done in the simplified one-dimensional case. In other words, the residual stress over the whole volume must be non-zero in real formed parts after springback. In order to compensate this disadvantage of the chord model, a new concept called quasi-plastic–elastic model (QPE model) was proposed (Sun and Wagoner, 2011). The QPE model was conceived from the two-yield-surface theory. One surface represents nonlinearity of elastic deformation, and, the other, the plastic deformation. This model was able to describe the complex unloading behavior more accurately and successfully applied to predict the springback in draw-bend test.

The objective of this paper is to enhance the modeling accuracy to a higher level than ever before. Thus, the main contribution of the present study is to present a unified theory for plasticity and elasticity for the finite element analysis of sheet metal forming process. The plasticity theory includes material's anisotropy and anisotropic hardening behavior, and the elasticity is not just constrained within the constant elastic properties but nonlinearity during unloading and reloading is considered as well. For this purpose, the two recently proposed modeling approaches, HAH and QPE models, will be combined, extended, numerically formulated and validated. The HAH model is able to predict the complex anisotropic behavior of sheet metals upon reverse loading, and the QPE model can precisely reproduce the nonlinear elastic unloading/reloading behavior. The main improvements developed in the present study are:

- The formulations for the QPE approach were generalized for any anisotropic yield function to be implemented into the FE modeling. The original QPE model used only von-Mises isotropic yield function for simplicity, thus analytical stress integration could be available. This constraint was removed in this study and the overall formulations were modified to make the theory more general.
- All numerical formulations were developed on the basis of the implicit algorithm. In the original QPE approach, the stress update algorithm and the QPE algorithm were based on isotropic quadratic yield function under three-dimensional condition, so that the derivation was made analytically. This is no longer valid for general non-quadratic anisotropic yield function and anisotropic hardening model like the HAH approach.
- The implementation was applied to the shell element formulation. In the original work, all springback simulations were done using continuum element. But, for future applications to realistic part forming simulations, the shell element is more efficient. Here, all formulations were developed under the plane stress condition.

In Section 2, the main features of the HAH and QPE model are reviewed. In Section 3, a finite element implementation of the constitutive models is investigated with a special attention to combining the two models. In Section 4, the developed numerical implementation is validated with simple boundary conditions. Finally, springback predictions in the U-draw bending are made by applying the current models and comparing with experiments. In particular, in addition to conventional U-draw bending with as-received sheet material, springback experiments with pre-strained sheets are also conducted in this study. The approach is illustrated using, two advanced high strength steels, DP780 and TRIP780 steel sheets.

2. Description of the constitutive models

2.1. Homogeneous yield function-based anisotropic hardening (HAH)

The following yield function, denoted as HAH, was proposed by Barlat et al. (2011)

$$\Phi(\boldsymbol{\sigma}) = \left(\phi^q + \phi_h^q\right)^{\frac{1}{q}} = \left(\phi^q + f_1^q\left|\hat{\mathbf{h}}^s : \mathbf{s} - \left|\hat{\mathbf{h}}^s : \mathbf{s}\right|\right|^q + f_2^q\left|\hat{\mathbf{h}}^s : \mathbf{s} + \left|\hat{\mathbf{h}}^s : \mathbf{s}\right|\right|^q\right)^{\frac{1}{q}} = \bar{\sigma}(\boldsymbol{\sigma}) \tag{1}$$

The yield function is a combination of a stable function ϕ and a fluctuating function ϕ_h. The stable component can be any isotropic or anisotropic yield function with first degree homogeneity. The fluctuating component is a function of the stress deviator $\mathbf{s}$, microstructure deviator $\hat{\mathbf{h}}^s$ and state variables, f_1 and f_2. The microstructure deviator $\hat{\mathbf{h}}^s$ which represents the previous deformation history is defined as the normalized quantity of the traceless tensor $\mathbf{h}^s$.

$$\hat{\mathbf{h}}^s = \frac{\mathbf{h}^s}{\sqrt{\frac{8}{3}\mathbf{h}^s : \mathbf{h}^s}} \tag{2}$$

The initial $\hat{\mathbf{h}}^s$ is the stress deviator $\mathbf{s}$ corresponding to the initial plastic deformation increment. The state variables f_1 and f_2 in Eq. (1) are functions of two variables, g_1 and g_2.

$$f_i = \left(g_i^{-q} - 1\right)^{\frac{1}{q}} \quad \text{for } i = 1 \text{ or } 2 \tag{3}$$

In the initial state, f_1 and f_2 are zero, and have no contribution to the yield surface. When the material is plastically deformed with a loading history, the state variables and the microstructure deviator are updated according to the following relationships.

$$\frac{dg_1}{d\bar{\varepsilon}} = \begin{cases} k_2\left(k_3\frac{H(0)}{H(\bar{\varepsilon})} - g_1\right) & \text{if} \quad \hat{\mathbf{h}}^s : \mathbf{s} \geqslant 0 \\ k_1\frac{g_4 - g_1}{g_1} & \text{if} \quad \hat{\mathbf{h}}^s : \mathbf{s} < 0 \end{cases} \tag{4}$$

$$\frac{dg_2}{d\bar{\varepsilon}} = \begin{cases} k_1\frac{g_3 - g_2}{g_2} & \text{if} \quad \hat{\mathbf{h}}^s : \mathbf{s} \geqslant 0 \\ k_2\left(k_3\frac{H(0)}{H(\bar{\varepsilon})} - g_2\right) & \text{if} \quad \hat{\mathbf{h}}^s : \mathbf{s} < 0 \end{cases} \tag{5}$$

$$\frac{dg_3}{d\bar{\varepsilon}} = \begin{cases} 0 & \text{if} \quad \hat{\mathbf{h}}^s : \mathbf{s} \geqslant 0 \\ k_5(k_4 - g_3) & \text{if} \quad \hat{\mathbf{h}}^s : \mathbf{s} < 0 \end{cases} \tag{6}$$

$$\frac{dg_4}{d\bar{\varepsilon}} = \begin{cases} k_5(k_4 - g_4) & \text{if} \quad \hat{\mathbf{h}}^s : \mathbf{s} \geqslant 0 \\ 0 & \text{if} \quad \hat{\mathbf{h}}^s : \mathbf{s} < 0 \end{cases} \tag{7}$$

$$\frac{d\hat{\mathbf{h}}^s}{d\bar{\varepsilon}} = \begin{cases} k\left(\hat{\mathbf{s}} - \frac{8}{3}\hat{\mathbf{h}}^s\left(\hat{\mathbf{h}}^s : \hat{\mathbf{s}}\right)\right) & \text{if} \quad \hat{\mathbf{h}}^s : \mathbf{s} \geqslant 0 \\ k\left(-\hat{\mathbf{s}} + \frac{8}{3}\hat{\mathbf{h}}^s\left(\hat{\mathbf{h}}^s : \hat{\mathbf{s}}\right)\right) & \text{if} \quad \hat{\mathbf{h}}^s : \mathbf{s} < 0 \end{cases} \tag{8}$$

where $\hat{\mathbf{s}}$ is the normalized quantity of $\mathbf{s}$ as in Eq. (2), $H(\bar{\varepsilon})$ is the classical isotropic hardening curve, and k and k_{1-5} are material constants. Two additional state variables, g_3 and g_4, are introduced in order to describe permanent softening. When the material has no permanent softening, k_4 or $k_5 = 0$ and $g_3 = g_4 = 1$.

The material parameters for the stable function in Eq. (1) and the monotonic hardening curve can be obtained by uniaxial tensile tests with various loading directions. Other mechanical tests such as bulge and disk compression tests can be used also if necessary, depending on the stable function. The parameters for the fluctuating part can be calculated from forward and reverse loading tests, for instance, uniaxial tension–compression or forward shear–reverse shear tests. More complex loading paths such as series of two-stage tension test can be also used for obtaining the parameters (Ha, 2012).

2.2. Quasi-plastic–elastic (QPE) model

Generalizing from uniaxial tension, the total strain increment $d\boldsymbol{\varepsilon}$ can be decomposed into three parts (Sun and Wagoner, 2011)

$$d\boldsymbol{\varepsilon} = d\boldsymbol{\varepsilon}_e + d\boldsymbol{\varepsilon}_p + d\boldsymbol{\varepsilon}_{QPE} \tag{9}$$

where $d\boldsymbol{\varepsilon}_e$ is the elastic strain, $d\boldsymbol{\varepsilon}_p$ is the plastic strain and $d\boldsymbol{\varepsilon}_{QPE}$ is the so-called QPE strain. Fig. 1(a) shows the stress–strain curve and a schematic view of the conceptual strain decomposition in Fig. 1(b) shows the continuous changes of slope during unloading and reloading. The elastic strain is calculated from the initial slope E_0 of the stress–strain curve as shown in Fig. 1(b). The other component of reversible strain, originating from the nonlinearity, is defined as the QPE strain. The QPE strain exhibits two fundamental properties, namely, recovery property energy dissipation.

In order to develop the QPE model, the concept of the two-yield-surface plasticity theory was applied. The inner and outer yield surfaces are the basic structure of the two-yield surface theory. The inner surface controls the nonlinear elastic behavior, and the outer surface governs the plastic behavior. When the QPE and the HAH models are used simultaneously, only the inner surface (QPE surface) translates in order to reproduce the nonlinear elastic behavior in the stress–strain curve during unloading and reloading.

Fig. 2 shows an example of the two-surface QPE model based on the HAH yield condition. From the two-surface theories (Dafalias and Popov, 1976; Geng and Wagoner, 2002; Lee et al., 2007; Yoshida et al., 2002), it is convenient to let the inner surface take the same shape as the outer surface.

$$\Theta_1(\boldsymbol{\sigma} - \boldsymbol{\alpha}, \bar{\varepsilon}) = \Phi_1(\boldsymbol{\sigma} - \boldsymbol{\alpha}) - H_1(\bar{\varepsilon}) = 0 \tag{10}$$

$$\Theta_2(\boldsymbol{\sigma}, \bar{\varepsilon}) = \Phi_2(\boldsymbol{\sigma}) - H_2(\bar{\varepsilon}) = 0 \tag{11}$$

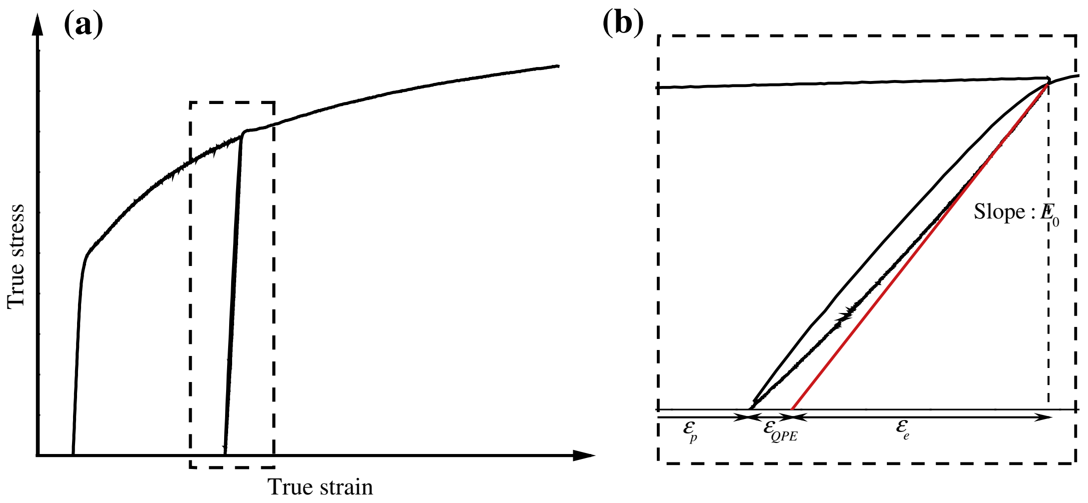

Fig. 1. (a) Stress–strain relation and (b) schematic view of the strain decomposition.

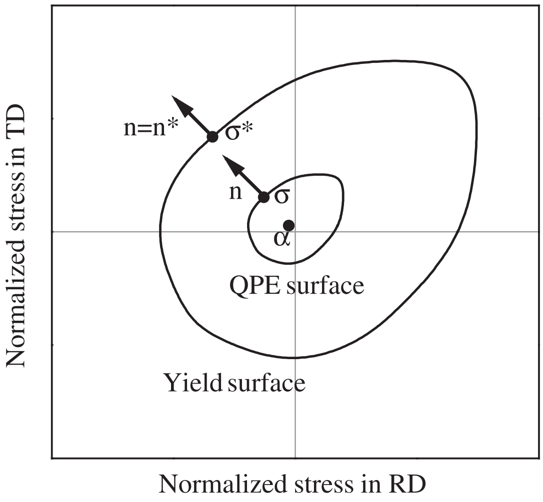

Fig. 2. Description of the QPE model coupled with the HAH model.

where H_1 and H_2 represent the size of the QPE and yield surfaces, Θ_1 and Θ_2, respectively. The tensor $\boldsymbol{\alpha}$ defines the center of the QPE surface. The variable $\bar{\varepsilon}$ is the equivalent plastic strain defined for the proposed yield function (see Barlat et al. (2011) and Lee et al. (2012a)). Given the applied stress $\boldsymbol{\sigma}$ (it may be anywhere inside the QPE surface for purely elastic deformation, or on the QPE surface, otherwise, as shown in Fig. 2), $\boldsymbol{\sigma}^*$ is the associated stress on the yield surface, sharing the same normal direction, i.e., $\mathbf{n} = \mathbf{n}^*$.

If the stress $\boldsymbol{\sigma}$ is inside the QPE surface Θ_1 and $d\boldsymbol{\sigma}$ projects inward, it is in elastic deformation mode. During this mode, the center $\boldsymbol{\alpha}$ and the size of each surface, i.e., H_1 and H_2, are unchanged. The total strain increment is, therefore, only the elastic strain increment.

$$d\boldsymbol{\varepsilon} = d\boldsymbol{\varepsilon}_e \tag{12}$$

$$d\boldsymbol{\sigma} = \mathbf{C}_0 : d\boldsymbol{\varepsilon}_e \tag{13}$$

where $\mathbf{C}_0$ is the classical, isotropic elastic stiffness tensor.

The QPE strain $d\boldsymbol{\varepsilon}_{QPE}$ occurs when the following three conditions are satisfied: (1) the applied stress $\boldsymbol{\sigma}$ is on the surface Θ_1, (2) the incremental stress $d\boldsymbol{\sigma}$ is outward ($d\boldsymbol{\sigma}: d\mathbf{n} > 0$), (3) the inner surface, Θ_1, and the yield surface, Θ_2, are not in contact. The total strain increment is, in this QPE mode,

$$d\boldsymbol{\varepsilon} = d\boldsymbol{\varepsilon}_e + d\boldsymbol{\varepsilon}_{QPE} \tag{14}$$

$$D\boldsymbol{\sigma} = \mathbf{C} : d\boldsymbol{\varepsilon} \tag{15}$$

where $\mathbf{C}$ is the elastic–QPE transition stiffness tensor as explained below.

The size of the inner surface is constant, but the location of its center moves during the QPE deformation. The evolution rule for the center of inner surface $\boldsymbol{\alpha}$ is as follows.

$$d\boldsymbol{\alpha} = d\mu(\boldsymbol{\sigma}^* - \boldsymbol{\sigma}) \tag{16}$$

$$\frac{\boldsymbol{\sigma} - \boldsymbol{\alpha}}{H_1} = \frac{\boldsymbol{\sigma}^*}{H_2} \tag{17}$$

An apparent modulus E, which represents the slope of stress–strain curve in uniaxial tension, is changed considering both the elastic and QPE strains.

$$E = E_0 - E_1\left(1 - \exp\left(-c\int \|d\boldsymbol{\varepsilon} - d\boldsymbol{\varepsilon}_p\|\right)\right) \tag{18}$$

where E_0 is the traditional Young's modulus, and E_1 and c are material coefficients. The integral in Eq. (18) is initiated whenever the new QPE loading process has taken place. The isotropic elastic stiffness matrix $\mathbf{C}$ is expressed by an apparent modulus for the QPE state.

$$\mathrm{C}_{ijkl} = \frac{vE}{(1+v)(1-2v)}(\delta_{ij}\delta_{kl}) + \frac{E}{(1+v)}(\delta_{ik}\delta_{jl} + \delta_{il}\delta_{jk}) \tag{19}$$

where δ_{ij} is the Kronecker delta and the Poisson's ratio ν is assumed to be constant.

If the inner surface Θ_1 is in contact with the yield surface Θ_2, necessarily, at the same stress point ($\boldsymbol{\sigma} = \boldsymbol{\sigma}^*$), and the incremental stress $d\boldsymbol{\sigma}$ is outward, plastic deformation occurs. The total strain increment is composed of the plastic, elastic and QPE strain increments. The size of inner surface increases in order to keep contact with the yield surface Θ_2, which evolves according to the plastic hardening law, Eq. (11). The size of the inner surface H_1 in Eq. (10) is assumed to follow the Voce equation with the equivalent plastic strain.

$$H_1(\bar{\varepsilon}) = A_1(1 - B_1 \exp(-D_1\bar{\varepsilon})) \tag{20}$$

where A_1, B_1 and D_1 are material coefficients which can be determined by monotonic loading–unloading–reloading experiments.

3. Combined QPE and HAH numerical formulations

The HAH and QPE models were implemented in the FE code using the material subroutines of the commercial software ABAQUS/Standard and Explicit (ABAQUS, 2010). The total strain increment, $\Delta\boldsymbol{\varepsilon}$, consists of the elastic $\Delta\boldsymbol{\varepsilon}^e$ and plastic $\Delta\boldsymbol{\varepsilon}^p$ parts.

$$\Delta\boldsymbol{\varepsilon} = \Delta\boldsymbol{\varepsilon}^e + \Delta\boldsymbol{\varepsilon}^p \tag{21}$$

The equivalent plastic strain increment, $\Delta\bar{\varepsilon}$, is obtained using the property of a first-degree homogeneous function $\bar{\sigma}(\boldsymbol{\sigma}) = \boldsymbol{\sigma} : \frac{\partial\bar{\sigma}}{\partial\boldsymbol{\sigma}}$ and the associated flow rule

$$\Delta\bar{\varepsilon} = \frac{\boldsymbol{\sigma} : \Delta\boldsymbol{\varepsilon}^p}{\bar{\sigma}(\boldsymbol{\sigma})} = \frac{\boldsymbol{\sigma} : \Delta\gamma\frac{\partial\bar{\sigma}}{\partial\boldsymbol{\sigma}}}{\bar{\sigma}(\boldsymbol{\sigma})} = \Delta\gamma\frac{\bar{\sigma}(\boldsymbol{\sigma})}{\bar{\sigma}(\boldsymbol{\sigma})} = \Delta\gamma \quad \text{and} \tag{22}$$

$$\Delta\boldsymbol{\varepsilon}^p = \Delta\gamma\frac{\partial\bar{\sigma}}{\partial\boldsymbol{\sigma}} = \Delta\bar{\varepsilon}\frac{\partial\bar{\sigma}}{\partial\boldsymbol{\sigma}} \tag{23}$$

The state variables in the HAH model are updated with Eqs. (4)–(8) when the equivalent plastic strain increment, $\Delta\bar{\varepsilon}$, is obtained. The unknown parameter $\Delta\bar{\varepsilon}$ can be found with numerous numerical schemes in the elasto-plastic formulations (De Borst and Feenstra, 1990; Dutko et al., 1993; Park and Lee, 1996; Simo and Hughes, 1998; Tugcu and Neale, 1999; Yoon et al., 1999b).

3.1. Fully implicit formulation: general closest point projection

The general closest point projection scheme has been commonly used upon considering the accuracy and efficiency in determining the solution. It leads a fully implicit procedure to impose the normality rule at the final iteration.

For a given $\Delta\boldsymbol{\varepsilon}_{n+1}$ at the current time step $n + 1$, a trial stress is calculated with the linear elasticity law

$$\boldsymbol{\sigma}^T_{n+1} = \boldsymbol{\sigma}_n + \mathbf{C}_n : \Delta\boldsymbol{\varepsilon}_{n+1} \tag{24}$$

where $\mathbf{C}_n$ is the elastic stiffness matrix, defined in Eq. (19) at the previous step, the superscript T denotes the trial state, and the subscripts n and $n + 1$ represent respectively the previous and present time steps.

When the trial stress satisfies the following condition,

$$\Theta_2(\boldsymbol{\sigma}^T_{n+1}, \bar{\varepsilon}_n) = \Phi_2(\boldsymbol{\sigma}^T_{n+1}) - H_2(\bar{\varepsilon}_n) > 0 \tag{25}$$

Plastic deformation occurs. The plastic flow residual $\mathbf{R}_1$, yield condition residual R_2 and other state variable residuals are specified from the previous Eqs. (4)–(8) and (23) for a sub-step k,

$$\mathbf{R}_1\left(\Delta\bar{\varepsilon}^{(k)}_{n+1}\right) = -\Delta\boldsymbol{\varepsilon}^{p^{(k)}}_{n+1} + \Delta\bar{\varepsilon}^{(k)}_{n+1}\frac{\partial\Phi_2\left(\boldsymbol{\sigma}^{(k)}_{n+1}\right)}{\partial\boldsymbol{\sigma}^{(k)}_{n+1}} \tag{26}$$

$$R_2\left(\Delta\bar{\varepsilon}^{(k)}_{n+1}\right) = \Phi_2\left(\boldsymbol{\sigma}^{(k)}_{n+1}\right) - H_2\left(\bar{\varepsilon}_n + \Delta\bar{\varepsilon}^{(k)}_{n+1}\right) \tag{27}$$

$$R_{l+2}\left(\Delta\bar{\varepsilon}^{(k)}_{n+1}\right) = g^{(k)}_{l,n+1} - g_{l,n} - \Delta g_l\left(\Delta\bar{\varepsilon}^{(k)}_{n+1}\right) \quad \text{for } l = 1 \sim 4 \tag{28}$$

$$\mathbf{R}_7\left(\Delta\bar{\varepsilon}^{(k)}_{n+1}\right) = \hat{\mathbf{h}}^{s(k)}_{n+1} - \hat{\mathbf{h}}^s_n - \Delta\hat{\mathbf{h}}^s\left(\Delta\bar{\varepsilon}^{(k)}_{n+1}\right) \tag{29}$$

By applying Taylor's expansion in Eqs. (26) and (27), the linearized residuals for the sub-step k at the current time are obtained as follows

$$\mathbf{R}_1\left(\Delta\bar{\varepsilon}^{(k)}_{n+1}\right) + \boldsymbol{\Xi}_n^{-1}\left(\Delta\bar{\varepsilon}^{(k)}_{n+1}\right) : \delta(\Delta\boldsymbol{\sigma}_{n+1})^{(k+1)} + \frac{\partial\Phi_2\left(\boldsymbol{\sigma}^{(k)}_{n+1}\right)}{\partial\boldsymbol{\sigma}^{(k)}_{n+1}}\delta(\Delta\bar{\varepsilon}_{n+1})^{(k+1)} = 0 \tag{30}$$

$$R_2\left(\Delta\bar{\varepsilon}^{(k)}_{n+1}\right) + \frac{\partial\Phi_2\left(\boldsymbol{\sigma}^{(k)}_{n+1}\right)}{\partial\boldsymbol{\sigma}}\delta(\Delta\boldsymbol{\sigma}_{n+1})^{(k+1)} - H_2'\left(\bar{\varepsilon}^{(k)}_{n+1}\right)\delta(\Delta\bar{\varepsilon}_{n+1})^{(k+1)} = 0 \tag{31}$$

where H_2' is the slope of the monotonic flow curve H_2. In Eqs. (30) and (31), the following quantities

$$\boldsymbol{\Xi}_n(\mathbf{x}) = \left(\mathbf{S}_n + \Delta\bar{\varepsilon}^{(k)}_{n+1}\frac{\partial^2\Phi_2\left(\boldsymbol{\sigma}^{(k)}_{n+1}\right)}{\partial\boldsymbol{\sigma}\partial\boldsymbol{\sigma}}\right)^{-1}, \quad \bar{\varepsilon}^{(k)}_{n+1} = \bar{\varepsilon}_n + \Delta\bar{\varepsilon}^{(k)}_{n+1}, \tag{32}$$

are introduced with $\mathbf{S}_n = \mathbf{C}_n^{-1}$ denoting the compliance tensor. Solving Eq. (30) for $\delta(\Delta\boldsymbol{\sigma}_{n+1})^{(k+1)}$ leads to

$$\delta(\Delta\boldsymbol{\sigma}_{n+1})^{(k+1)} = \boldsymbol{\Xi}_n\left(\Delta\bar{\varepsilon}^{(k)}_{n+1}\right) : \left(-\mathbf{R}_1\left(\Delta\bar{\varepsilon}^{(k)}_{n+1}\right) - \frac{\partial\Phi_2(\boldsymbol{\sigma}^{(k)}_{n+1})}{\partial\boldsymbol{\sigma}^{(k)}_{n+1}}\delta\left(\Delta\bar{\varepsilon}^{(k+1)}_{n+1}\right)\right) \tag{33}$$

By substituting Eq. (33) into Eq. (31) the variation of the equivalent plastic strain increment $\delta\Delta\bar{\varepsilon}$ becomes

$$\delta(\Delta\bar{\varepsilon}_{n+1})^{(k+1)} = \frac{R_2\left(\Delta\bar{\varepsilon}^{(k)}_{n+1}\right) - \mathbf{R}_1\left(\Delta\bar{\varepsilon}^{(k)}_{n+1}\right) : \boldsymbol{\Xi}_n\left(\Delta\bar{\varepsilon}^{(k)}_{n+1}\right) : \frac{\partial\Phi_2\left(\boldsymbol{\sigma}^{(k)}_{n+1}\right)}{\partial\boldsymbol{\sigma}}}{\frac{\partial\Phi_2\left(\boldsymbol{\sigma}^{(k)}_{n+1}\right)}{\partial\boldsymbol{\sigma}^{(k)}_{n+1}} : \boldsymbol{\Xi}_n\left(\Delta\bar{\varepsilon}^{(k)}_{n+1}\right) : \frac{\partial\Phi_2\left(\boldsymbol{\sigma}^{(k)}_{n+1}\right)}{\partial\boldsymbol{\sigma}^{(k)}_{n+1}} + H_2'\left(\bar{\varepsilon}^{(k)}_{n+1}\right)} \tag{34}$$

Finally, the plastic multiplier and the other plastic state variables are updated for step $(k+1)$ with Eqs. (4)–(8) and the updated effective and plastic strains.

$$\Delta\bar{\varepsilon}^{(k+1)}_{n+1} = \Delta\bar{\varepsilon}^{(k)}_{n+1} + \delta(\Delta\bar{\varepsilon}_{n+1})^{(k+1)} \tag{35}$$

$$\boldsymbol{\varepsilon}^{p^{(k+1)}}_{n+1} = \boldsymbol{\varepsilon}^{p^{(k)}}_{n+1} + \delta\left(\Delta\bar{\varepsilon}_{n+1}\frac{\partial\Phi_2(\boldsymbol{\sigma}_{n+1})}{\partial\boldsymbol{\sigma}_{n+1}}\right)^{(k)} \tag{36}$$

This iterative cycle continues until the size of each residual R_i (i = 1–7) becomes smaller than a prescribed tolerance (e.g., 10^{-6}).

In the fully implicit formulation with non-quadratic yield function, a divergence problem may occur for some stress state. In such case, the multi-step return mapping approach proposed by Yoon et al. (1999a) can be efficiently introduced. Moreover, for this particular distortional hardening model another sub-stepping algorithm has been proposed to calculate the gradient of distorted yield surface to relieve another type of divergence. For more details on the whole derivations and analysis with iso-error map scheme, refer to Lee et al. (2012c).

3.2. Semi-explicit formulation: cutting-plane algorithm

Ortiz and Simo (1986) proposed the cutting-plane algorithm to eliminate the need for computing the second derivative in the calculation of the plastic strain increment $\Delta\bar{\varepsilon}$, Eq. (32). From the consistency condition for plastic yielding,

$$\Theta_2 = \Phi_2(\boldsymbol{\sigma} + \Delta\boldsymbol{\sigma}, f_1 + \Delta f_1, f_2 + \Delta f_2, \hat{\mathbf{h}}^s + \Delta\hat{\mathbf{h}}^s) - H_2(\bar{\varepsilon} + \Delta\bar{\varepsilon}) = 0 \tag{37}$$

Applying the Taylor's expansion,

$$\Theta_2 + \Delta\Theta_2 = \Theta_2 + \frac{\partial\Theta_2}{\partial\Delta\bar{\varepsilon}}\delta(\Delta\bar{\varepsilon}) = 0 \tag{38}$$

$$\delta(\Delta\bar{\varepsilon}) = \frac{-\Theta_2}{\frac{\partial\Theta_2}{\partial\boldsymbol{\sigma}}\frac{\partial\boldsymbol{\sigma}}{\partial\Delta\bar{\varepsilon}} + \frac{\partial\Theta_2}{\partial H_2}\frac{\partial H_2}{\partial\Delta\bar{\varepsilon}}} \quad \text{with} \quad \frac{\partial\Theta_2}{\partial\boldsymbol{\sigma}} = \frac{\partial\Phi_2}{\partial\boldsymbol{\sigma}}, \frac{\partial\Theta_2}{\partial \mathrm{H}_2} = -1 \quad \text{and} \quad \frac{\partial\Theta_2}{\partial\Delta\bar{\varepsilon}} = -\mathbf{C}\frac{\partial\Phi_2}{\partial\boldsymbol{\sigma}} \tag{39}$$

If the trial stress defined in Eq. (24) meets the condition of $\Theta_2 > 0$ at the current time step $n + 1$, the variation of equivalent plastic increment for sub-step k is obtained from Eq. (39),

$$\delta(\Delta\bar{\varepsilon}_{n+1})^{(k+1)} = \frac{\Theta_2}{\frac{\partial\Phi_2\left(\boldsymbol{\sigma}^{(k)}_{n+1}\right)}{\partial\boldsymbol{\sigma}}C_n\frac{\partial\Phi_2\left(\boldsymbol{\sigma}^{(k)}_{n+1}\right)}{\partial\boldsymbol{\sigma}^{(k)}_{n+1}} + H_2'\left(\bar{\varepsilon}^{(k)}_{n+1}\right)} \tag{40}$$

Then, the plastic multiplier and other state variables are updated for step $(k+1)$ with Eqs. (4)–(8), (35) and (36). The iteration continues until $|\Theta_2| < \mathrm{TOL}$ (a prescribed numerical tolerance) is satisfied. The gradient of the yield function, $\frac{\partial \Phi_2}{\partial \boldsymbol{\sigma}}$, should be carefully determined by the multi-step Newton–Raphson method proposed by Lee et al. (2012a) because of the distortion of the yield surface in the HAH model.

3.3. Implicit elastic–QPE transition algorithm

If the trial stress given in Eq. (24) satisfies the following condition

$$f_2(\boldsymbol{\sigma}^T_{n+1}, \bar{\varepsilon}_n) = \phi_2(\boldsymbol{\sigma}^T_{n+1}) - H_2(\bar{\varepsilon}_n) \leqslant 0 \tag{41}$$

the trial state is considered as elastic and the stress is either purely elastic or QPE. When both Eq. (41) and

$$f_1(\boldsymbol{\sigma}^T_{n+1} - \boldsymbol{\alpha}_n, \bar{\varepsilon}_n) = \phi_1(\boldsymbol{\sigma}^T_{n+1} - \boldsymbol{\alpha}_n) - H_1(\bar{\varepsilon}_n) < 0 \tag{42}$$

are satisfied, the trial stress is purely elastic and the stress and the center $\boldsymbol{\alpha}$ are updated as

$$\boldsymbol{\sigma}_{n+1} = \boldsymbol{\sigma}^T_{n+1}, \quad \boldsymbol{\alpha}_{n+1} = \boldsymbol{\alpha}_n \tag{43}$$

If the condition in Eq. (42) is not met, the trial stress is in the QPE state. In this case the trial stress is located outside of the inner surface and inside of the yield surface. The elastic stiffness matrix $\mathbf{C}_{n+1}$ is updated with Eqs. (18) and (19) and the updated stress and the center $\boldsymbol{\alpha}$ are calculated with Eqs. (16) and (17).

$$\boldsymbol{\sigma}_{n+1} = \boldsymbol{\sigma}_n + \mathbf{C}_{n+1} : \Delta\boldsymbol{\varepsilon}_{n+1} \tag{44}$$

$$\boldsymbol{\alpha}_{n+1} = \boldsymbol{\alpha}_n + d\boldsymbol{\alpha}_n = \boldsymbol{\alpha}_n + d\mu\left(\frac{R_2 - R_1}{R_1}\boldsymbol{\sigma}_n - \frac{R_2}{R_1}\boldsymbol{\alpha}_n\right) \tag{45}$$

In order to obtain the value $d\mu$, the Newton–Raphson method is used under the consistency condition

$$f_1 = \phi_1(\mathbf{r}_{n+1}) - H_1(\bar{\varepsilon}_n) = 0 \tag{46}$$

where $\mathbf{r}_{n+1}$ is $\boldsymbol{\sigma}_{n+1} - \boldsymbol{\alpha}_n - d\boldsymbol{\alpha}_n$.

By applying Talyor's expansion,

$$f_1 + \frac{\partial f_1}{\partial \mathbf{r}_{n+1}}\frac{\partial \mathbf{r}_{n+1}}{d(d\mu)}d(d\mu) = 0 \tag{47}$$

$$d(d\mu) = \frac{-f_1}{\frac{\partial f_1}{\partial \mathbf{r}_{n+1}}\frac{\partial \mathbf{r}_{n+1}}{d(d\mu)}} \tag{48}$$

where $\frac{\partial \mathbf{r}_{n+1}}{d(d\mu)} = \frac{R_2 - R_1}{R_1}\boldsymbol{\sigma}_n - \frac{R_2}{R_1}\boldsymbol{\alpha}_n$. Note that the derivative of the inner surface, $\frac{\partial f_1}{\partial \mathbf{r}_{n+1}}$, is calculated in the same way as $\frac{\partial \Phi_2}{\partial \boldsymbol{\sigma}}$ in Eq. (40).

Iterations continue until the value $d(d\mu)$ becomes within a prescribed tolerance. $\boldsymbol{\alpha}_{n+1}$ is obtained after substituting the solution of Eqs. (46)–(48) into (45).

4. Applications

The parameters for the QPE and HAH models were determined by the Nelder and Mead simplex algorithm (1965). This algorithm is a robust method for parameter optimization because it does not require the first derivative of the objective function in contrast to the frequently used nonlinear least-square or Newton–Raphson methods. In order to optimize N parameters, $N+1$ arbitrary initial sets are determined. Because the simplex algorithm can give local optimized values, several sets of initial estimates are tried. The objective function is the sum of absolute difference between the experimental data and the predicted results at each iteration. The iteration continues until the standard deviation, is less than a prescribed numerical tolerance, e.g., 10^{-6}.

$$\sqrt{\frac{\sum_{i=1}^{N+1}(\theta_i - \theta_{\mathrm{mean}})}{N+1}} \leqslant TOL \tag{49}$$

where θ_i is the objective function value and θ_{mean} is the average value from the objective function.

4.1. Prediction of 1-D stress–strain curve for TRIP780 and DP780 steel sheets

For the experimental part of this study, a 1.4 mm thick DP780 dual-phase steel sheet and a 1.2 mm thick TRIP780 (transformation-induced plasticity) steel sheet were selected. The basic mechanical properties of these materials are listed in

Table 1
Mechanical properties of TRIP780 and DP780 steel sheets.

Material	Direction (from the RD)	E_0, GPa	Poisson's ratio	[a]Yield stress, MPa	Unif. Elong.	Total Elong.	r value ($\varepsilon_p = 0.1$)
TRIP780	0° (RD)	198.5	0.3	486	0.17	0.22	0.79
	45°			493	0.17	0.23	0.93
	90° (TD)			500	0.16	0.21	0.82
	Bulge test			525			0.83[b]
DP780[c]	0°	198.8	0.3	452	0.13	0.20	0.78

[a] Yield stress: 0.2% offset.
[b] r value is defined in balanced biaxial tension test as $\frac{d\varepsilon_{TD}}{d\varepsilon_{RD}}$.
[c] Material data were taken from the NUMISHEET2011 benchmark report.

Table 1. The uniaxial tension and in-plane tension–compression–tension (TCT) tests for DP780 were taken from the NUMISHEET (2011) benchmark report. In-plane TCT experiments were conducted for five different reversal strains, approximately 2%, 5%, 7%, 9% and 11%. For TRIP780, uniaxial tension tests were conducted with an MTS universal machine. Forward–reverse shear tests were performed using the equipment described by Lee et al. (2012a).

The monotonic stress–strain curves under loading–unloading–reloading were also conducted for TRIP780 steel sheet, Fig. 3(a). The TRIP780 steel sheet sample exhibits nonlinear stress–strain behavior and energy dissipation during elastic unloading and reloading. Fig. 3(b) and (c) show the amount of the elastic and QPE strains, and the dissipated energy at each loading–unloading–reloading loop with respect to the unloading stress. The dissipated energy and QPE strain were observed to increase with strain.

The FE simulations were carried out with ABAQUS/Standard and the user material subroutine UMAT. The 4-nodes shell element with reduced integration point (S4R) was adopted. In the applications, the non-quadratic anisotropic yield function Yld2000-2d (Barlat et al., 2003) was applied as a stable component in Eq. (1), except as otherwise indicated.

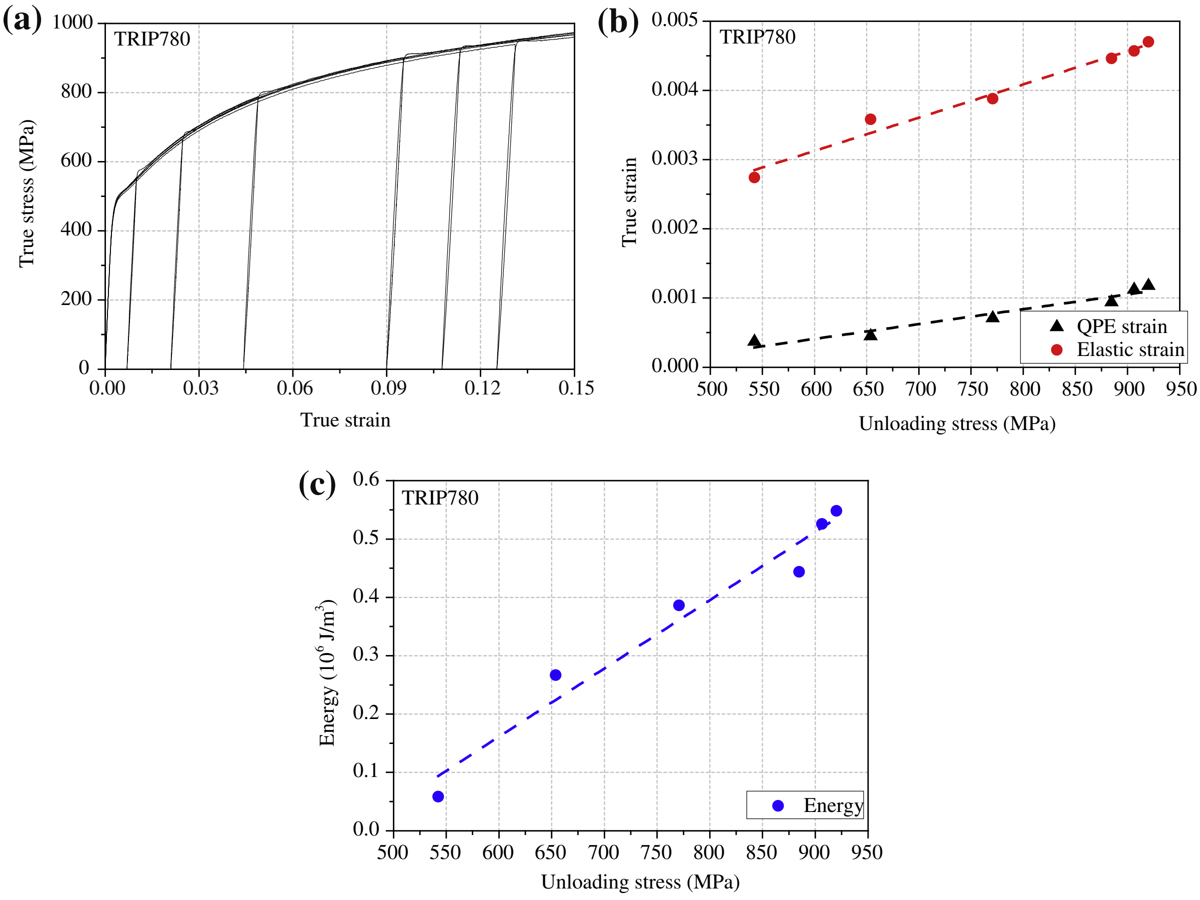

Fig. 3. (a) Results of uniaxial stress–strain curves for TRIP780 steel sheet under loading–unloading–reloading cycle; (b) QPE strain and elastic strain with respect to the unloading stress; and (c) dissipated energy during loading–unloading with respect to the unloading stress.

The uniaxial tensile deformation behavior for TRIP780 steel sheet was not well approximated with either the Swift or Voce hardening laws. Therefore, the combined Swift–Voce or Hollomon–Voce isotropic hardening law was used for the yield surface Θ_2 in Eq. (11) (Sung et al., 2010).

$$H_2(\bar{\varepsilon}) = L(K(\varepsilon_0 + \bar{\varepsilon})^n) + (1 - L)(A_2(1 - B_2 \exp(-D_2\bar{\varepsilon}))) \tag{50}$$

where $K, \varepsilon_0, n, A_2, B_2, D_2$ are material parameters and L is a weight parameter. Fig. 4 compares the experimental and predicted flow stress curves for the optimum parameters listed in Table 2. For DP780 steel sheet, the Swift hardening law was adopted and the corresponding material parameters are listed in Table 3.

Additionally, the chord elastic modulus at various pre-strains, determined as the slope of a straight line from stress at unloading to zero, is described as a continuous function of pre-strain as follows

$$E = E_0 - (E_0 - E_a)(1 - \exp(-\xi\bar{\varepsilon})) \tag{51}$$

where E_0, E_a and ξ are material parameters and listed in Tables 2 and 3. The first two are the initial and saturated Young's moduli, respectively as shown in Fig. 5. In the early stage of equivalent plastic strain the chord elastic modulus of DP780 steel sheet decreases faster than that of TRIP780 steel sheet, as indicated by Fig. 5.

The coefficients of the HAH and QPE models, listed in Tables 2 and 3, were obtained from the experimental TCT and loading–unloading–reloading curves. Because there is a difference of plastic strain between the HAH model with or without the QPE, the corresponding coefficients are slightly different. Figs. 6 and 7 shows the predictions of the stress–strain curves for forward-reverse shear and TCT tests using the HAH model combined either with the chord or QPE models. These figures indicate that the Bauschinger effect, transient behavior and permanent softening are well captured by the HAH model.

Fig. 8 shows the overall approximation of the unloading–reloading experimental data for the TRIP780 steel sheet with the QPE model. The QPE model captured the nonlinear behavior for all loading–unloading–loading loops, although the QPE parameters were calculated using the sixth unloading–reloading cycle. Fig. 9 represents the approximation of experimental data for the DP780 steel sheet at 11% pre-strain by the QPE model. Again, the QPE model captured the nonlinear elastic behavior satisfactorily.

An error parameter was defined as

$$e_a(\%) = \frac{\left(\sum_{i=1}^{N} \frac{\left|\theta^i_{\text{model}} - \theta^i_{\text{exp}}\right|}{\theta^i_{\text{exp}}}\right)}{N} \times 100 \tag{52}$$

where N is the number of points, and θ_{model} and θ_{exp} are the strains taken at the same stress level from the simulation and experiment, respectively. e_a provided, in Table 4, quantitative value of the error between predicted and experimental loops in Fig. 8. The errors with the chord modulus were about four times as large as those of the QPE model at every strain level.

4.2. Prediction of springback in U-draw bending

In order to validate the proposed models in U-draw bending, as received and 8% pre-strained specimens, were prepared for TRIP780 steel sheet. For the base material, 350 mm (RD) by 45 mm (TD) rectangular shaped specimens were prepared as shown in Fig. 10(a). For the pre-strained material 450 mm by 45 mm, specimens were first deformed in tension with a MTS universal material testing machine. A 28 mm grip displacement was applied at a strain rate of about 10^{-3}/s and resulted in approximately 8% engineering strain schematically represented at the specimen center as measured with an extensometer in Fig. 10(b). U-draw bending tests, in Fig. 11(a), were conducted with a holding force of 20 kN. The punch velocity was

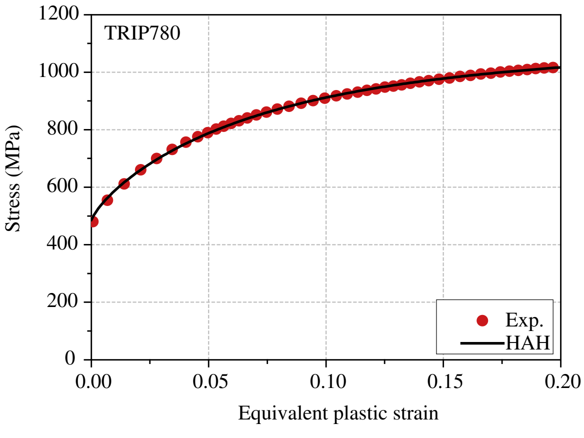

Fig. 4. Equivalent plastic stress–strain curves for TRIP780 steel sheet.

Table 2
Constitutive model parameters for TRIP780 steel sheet.

Chord model	E_a (GPa)	ξ							
	161.3	59.1							
QPE model	A_1 (MPa)	B_1	D_1	E_0 (MPa)	E_1 (MPa)	C			
	196.96	0.523	4.3	198500	95000	354			
Hardening law	K (MPa)	ε_0	n	A_2 (MPa)	B_2	D_2	L		
	1424.2	0.003	0.20	1033.3	0.505	15	0.35		
HAH – Chord	q	k	k_1	k_2	k_3	k_4	k_5		
	2	30	33	80	0.6	0.9	10		
HAH – QPE	q	k	k_1	k_2	k_3	k_4	k_5		
	2	30	30	80	0.6	0.9	10		
Yld2000-2d	Exponent	α_1	α_2	α_3	α_4	α_5	α_6	α_7	α_8
	6	1.007	0.947	0.943	1.001	1.023	1.054	1.004	1.033

Table 3
Constitutive model parameters for DP780 steel sheet.

Chord model	E_a (GPa)	ξ							
	152.1	96.5							
QPE model	A_1 (MPa)	B_1	D_1	E_0 (MPa)	E_1 (MPa)	C			
	96.9	0	0	198800	95000	254			
Hardening law	K (MPa)	ε_0	n						
	1280.23	0.0008	0.146						
HAH – Chord	q	k	k_1	k_2	k_3	k_4	k_5		
	2	30	100	90	0.6	0.9	30		
HAH – QPE	q	k	k_1	k_2	k_3	k_4	k_5		
	2	30	125	90	0.6	0.9	30		
Yld2000-2d	Exponent	α_1	α_2	α_3	α_4	α_5	α_6	α_7	α_8
	6	0.928	1.024	0.962	0.988	1.004	0.917	1.004	1.032

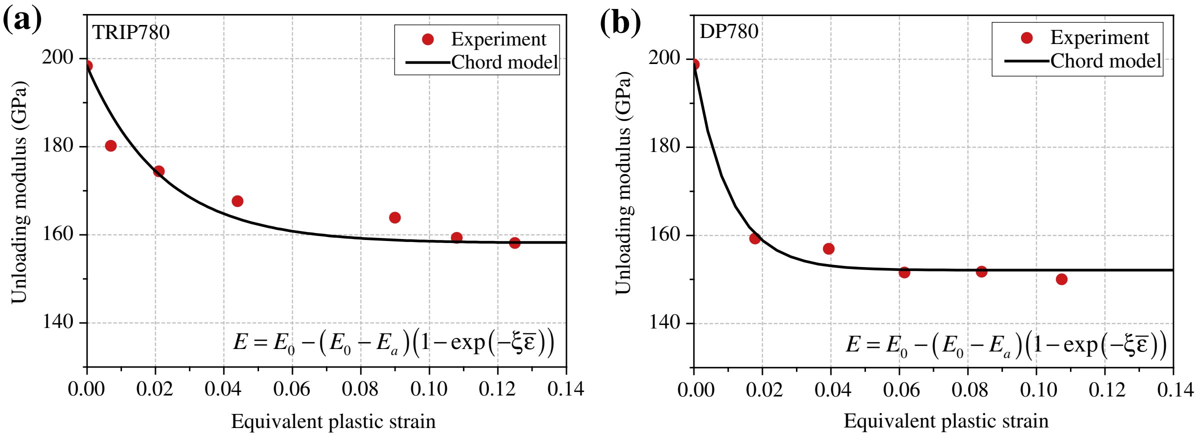

Fig. 5. Chord elastic modulus as a function of equivalent plastic strain for (a) TRIP780 and (b) DP780 steel sheets.

1.0 mm/s and the stroke was 70 mm. For lubrication, P340 N (rust-preventive oil) was applied to the surface of the specimens and tools. The Coulomb friction law was assumed with the coefficient 0.14 between the blank and the tools. After the tests, the springback profiles and the three parameters proposed in the NUMISHEET (1993) benchmark, as shown in Fig. 11(a), were determined.

For the DP780 steel sheet, the condition for U-draw bending was slightly different from that of TRIP780 (NUMISHEET, 2011). 360 mm (RD) by 30 mm (TD) rectangular specimens were used for both as-received and pre-strained 7.8% materials. Fig. 11(b) shows the dimension of the tools and three parameters measured after springback according to NUMISHEET 2011.

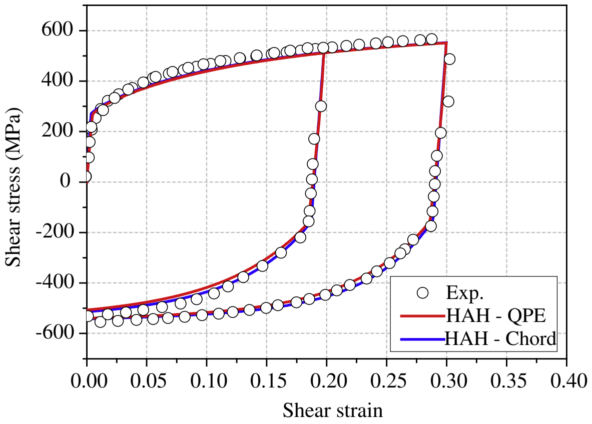

Fig. 6. Forward and reverse shear stress–strain curves for TRIP780 steel sheet.

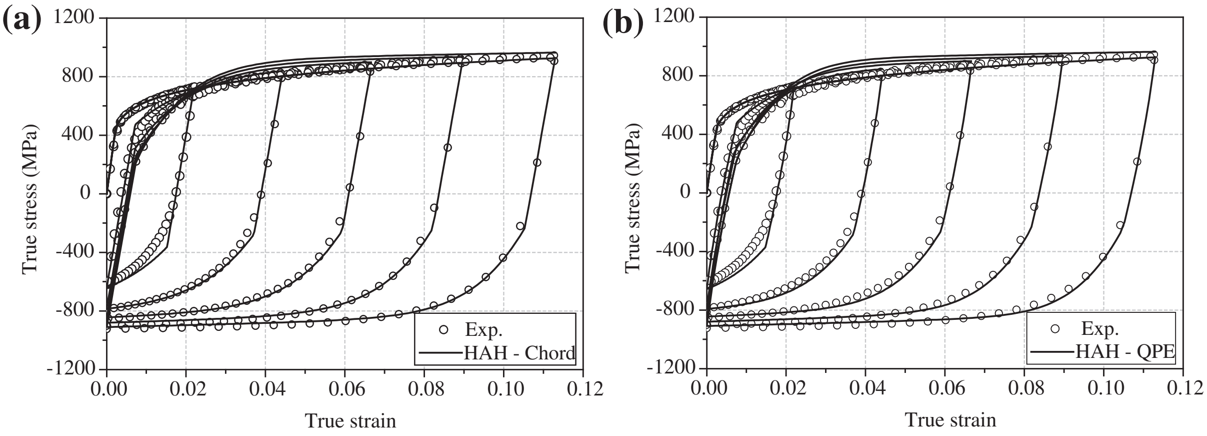

Fig. 7. Stress–strain curves for tension–compression–tension condition for DP780, (a) the HAH-Chord and (b) the HAH–QPE.

The holding force was 2.94 kN. The punch velocity was set to 1 mm/s and the punch stroke to 71.8 mm. The Coulomb friction law was assumed with the coefficient 0.1 between the blank and the tools.

The finite element simulations for the U-draw bending process were performed with ABAQUS implicit and explicit codes. The implicit code was used for solving pre-straining and springback, and the explicit code was used for solving the U-draw bending forming stage. The semi-implicit algorithm was used for the forming simulation, while the fully implicit algorithm was used for the springback. The main reason why the semi-implicit algorithm (or cutting plane algorithm) is applied for the forming simulation is to relieve computational complex but without deteriorating the accuracy of the calculated stresses. It has been well known that the cutting plane algorithm does not need the derivative of plastic strain rate (or second derivative of yield surface with respect to the stress) and does consider only consistency. However, this simplification does not follow the minimum plastic work path under the incremental deformation theory and also violates the normality condition at the current state. However, when the algorithm is coupled with explicit FE code, the solution by the tangent cutting plane algorithm seems to converge to the solution by the fully implicit algorithm due to its tiny time step for the stabilized solution. This approach might be a good compromise in both accuracy and computational efficiency. Although the accuracy of the cutting plane algorithm is guaranteed in the explicit time integration scheme, it should be carefully used for the springback simulation. In the implicit FE scheme, the time step is much larger than that of the explicit scheme, and most of commercial (or even in-house) FE codes use automatic time stepping strategy. Preliminary analyses to validate the accuracy of the two stress integration algorithms, which include the analyses of *r*-value, stress, and error maps showed that fully implicit stress integration algorithm should be preferably used for accurate springback results. For more details, refer to either Lee et al.(2012c) for HAH approach or Cardoso and Yoon (2009) for isotropic–kinematic hardening approach.

Taking symmetry into consideration, only a quarter of the whole blank was modeled. The tools were constructed with analytical rigid body surface. The blank was modeled using shell element with reduced integration point (S4R) and 9 integration points through thickness. The mesh size, determined through convergence tests, was 1 mm by 1.5 mm and 0.5 mm by 0.75 mm (length by width) for TRIP780 and DP780 steel sheets, respectively.

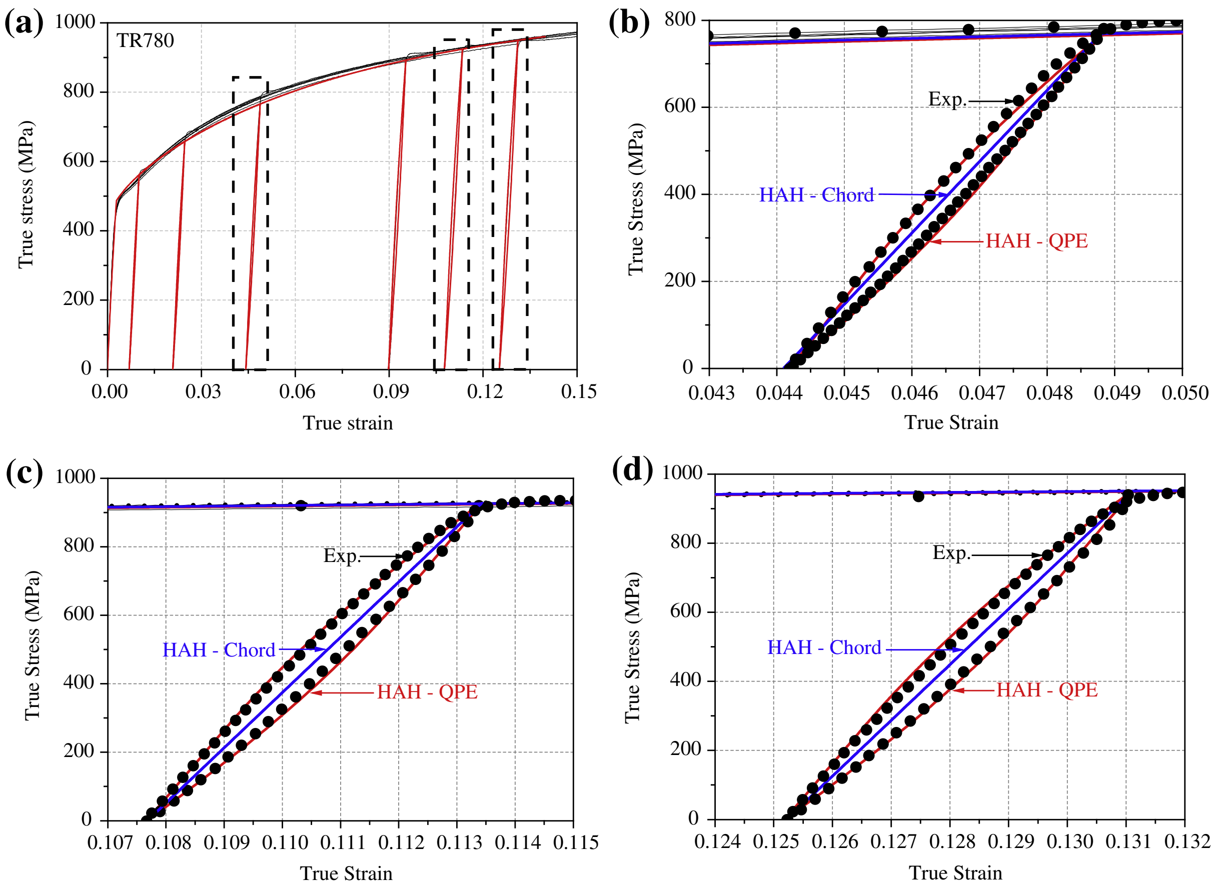

Fig. 8. (a) QPE model predictions with the experimental data for loading–unloading–reloading test; (b) third cycle with the simulation results; (c) fifth cycle with the simulation result; and (d) sixth cycle with the simulation results.

For DP780 steel sheet, the final experimental and predicted profiles after springback for as-received and pre-strained materials are presented in Fig. 12. For comparison purpose, the simulation result for isotropic hardening with the chord model (IH-Chord) is also shown in Fig. 12. In Fig. 13, detailed values of the three springback parameters are compared. This Fig. 12 indicates that the chord model tends to over-predict springback. The QPE model also over-estimates springback in the case of as-received materials, but the difference is smaller than that of the chord model. In particular, in the sidewall curl region, the QPE predictions are in good agreements with experimental data. Because the side-wall curl region experiences bending, unbending and stretching during forming, it is important for the plastic hardening models to capture the Bauschinger effect, transient behavior and permanent softening. Nevertheless, the simulations show that not only plastic hardening but also elastic models are important in predicting springback phenomena accurately.

For TRIP780 steel sheet, larger springback predictions are observed as shown in Fig. 14. The classical isotropic hardening model (IH-Chord) in Fig. 14 over-estimates the experimental springback in both cases. Fig. 14(a) shows that the HAH model tends to predict larger springback than the actual amount for as-received material. In contrast, the springback predicted with the HAH model is in favorable agreement with the measurements for the pre-strained samples. The predictions using the QPE model are in slightly better agreement with the experiments than those with the chord model (see Fig. 15).

5. Discussion

In the previous section, the proposed material models and FE implementation were well validated for the U-draw bending springback of two AHSS with similar strength. In terms of the prediction capability, an interesting result was found; i.e., simulated springback was always over-predicted but even more so with the as-received TRIP780 steel sheet. Two factors can be considered to explain these results, namely, friction and temperature. In the present study, the Coulomb friction law was assumed and the friction coefficient was measured using a standard tester. However, this simple friction approach might not be very accurate because the friction behavior is influenced by other factors such as the strain rate, pressure and temperature (Darendeliler et al., 2002; Matuszak, 2000). The topic of friction modeling will be further investigated as a follow-up of the present research.

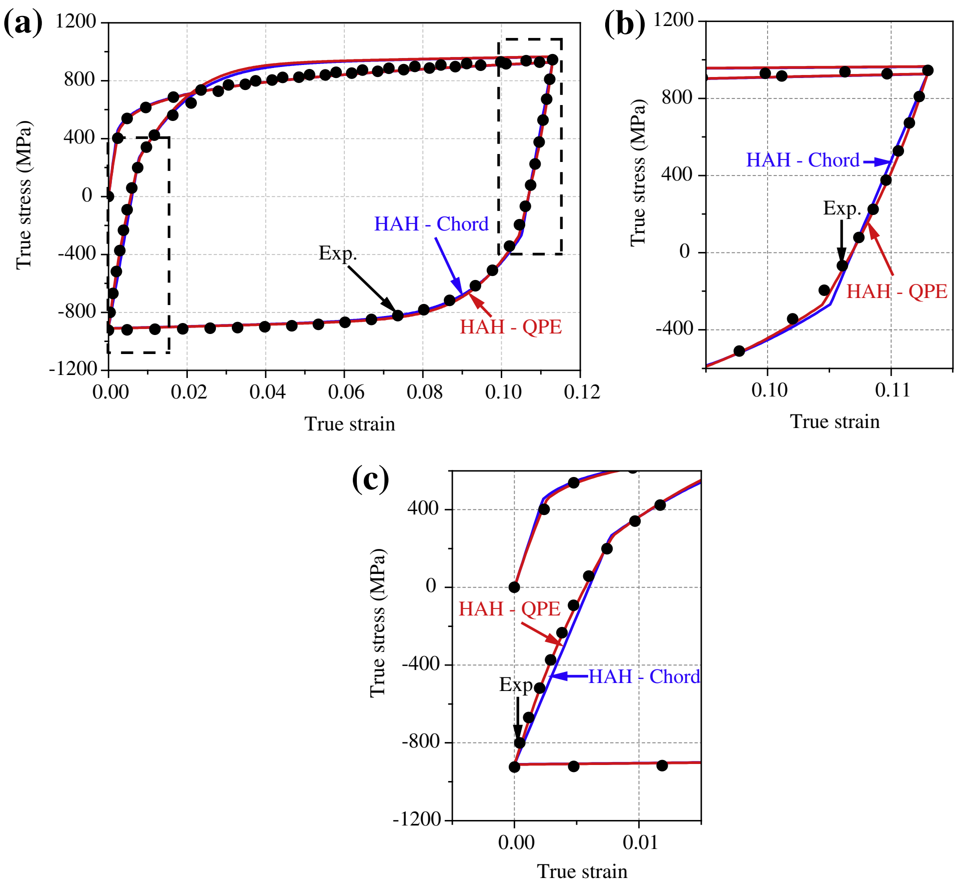

Fig. 9. (a) QPE model prediction for DP780 for the TCT test with 11% pre-strain; (b) first unloading with the simulation results; (c) second unloading with the simulation results.

Table 4
Errors in unloading–reloading loop prediction in Fig. 8.

Pre-strain	5% (Fig. 8(b))	11% (Fig. 8(c))	13% (Fig. 8(d))
Error in Chord model	0.41%	0.23%	0.2%
Error in QPE model	0.12%	0.04%	0.05%

Kim et al. (2009) found that the temperature of AHSS sheet during forming increases up to a significant level. In order to roughly estimate the temperature rise, a coupled thermal–mechanical FE analysis of U-draw bending was carried out for the as-received TRIP780 sheet. To simplify the problem, only isotropic hardening with von-Mises yield function was used for the material description. The result of this analysis showed that the average temperature for the blank in the die corner and side wall region increased to about 55 °C from room temperature (RT). Therefore, bulge tests under isothermal condition were carried out for three different temperatures namely, 20, 50 and 100 °C, and the resulting stress–strain curves are shown in Fig. 16. For both materials, as temperature increases, the flow stress decreases by an amount which is significant for the TRIP780 steel sheet. For this material, this is due to the combined effect of temperature increase and lower transformation kinetics (Lee et al., 2010). For DP780, the flow stress drop is only due to the usual temperature effect. In addition, the transformed volume fraction of austenite in TRIP780 steel sheet measured by magnetic saturation method is also presented in Fig. 16(b). The fraction of austenite transformed after uniaxial tension at room temperature saturates after about 10% plastic strain. Considering this temperature effect on the flow stress, springback simulations were performed again for DP780 and TRIP780 steel sheets as explained in the next paragraph.

For DP780 steel sheet, all FE simulations in Fig. 12 were performed using the stress–strain curve measured at room temperature T_R, which follows the segment O–B in Fig. 17(a). However, under the forming condition used in this study, there is a temperature increase of about 55 °C, which is denoted as T^* in the schematic drawing of Fig. 17. Therefore, in the real forming experiment, the final stress of the blank before springback is likely to be close to B_1 for the as-received material. For the pre-strained material, the situation is slightly different. The stress–strain response during pre-strain follows segment O–A because tension was applied at room temperature. Point U is the start point of the U-draw bending for the pre-strained

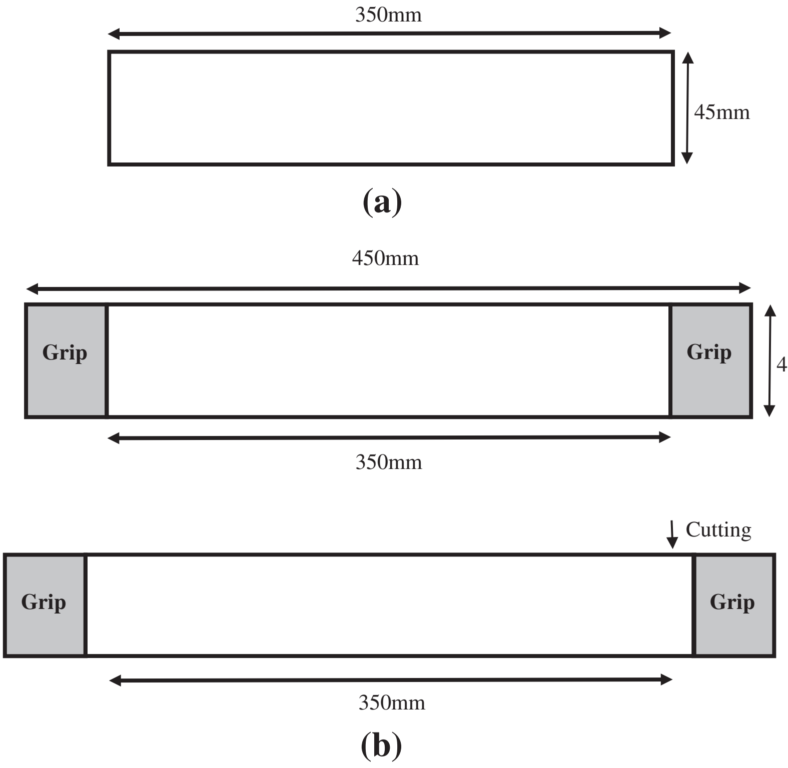

Fig. 10. TRIP780 specimens for U-draw bending (a) as-received and (b) pre-strained by 8%.

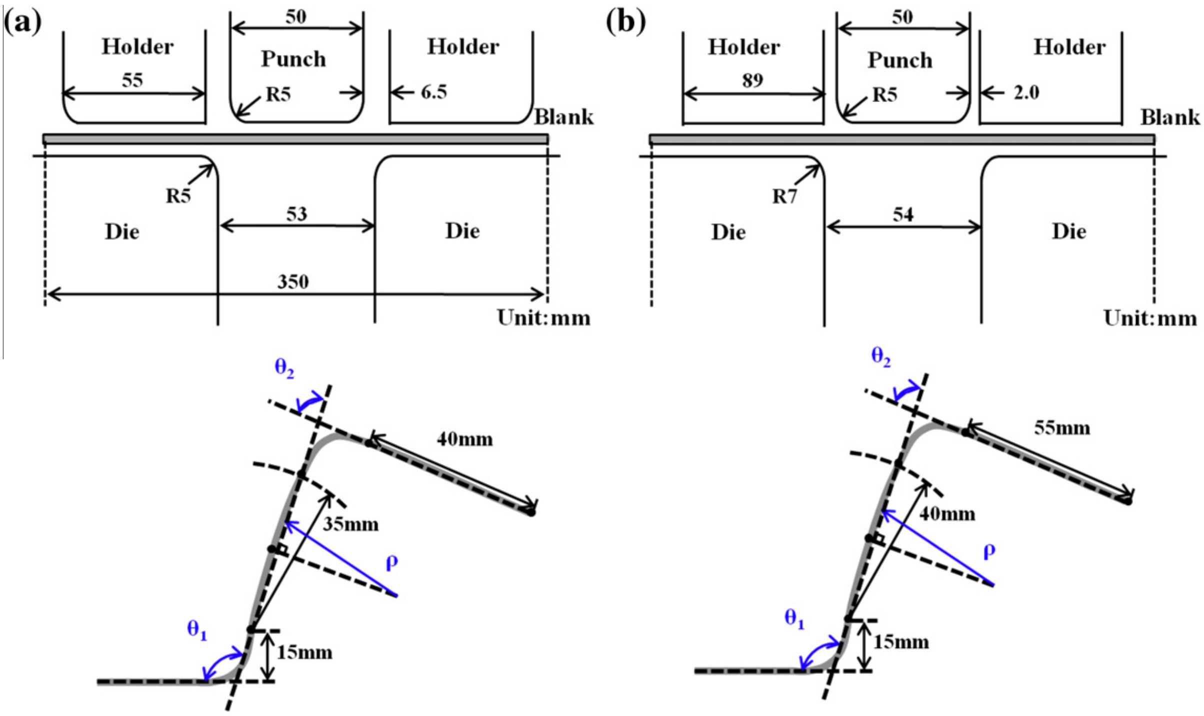

Fig. 11. Tool geometry and measurement of springback for (a) TRIP780 and (b) DP780 steel sheets.

material. After U-draw bending, as a rough simplification the flow stress is assumed to be close to the segment A_1–B_1. Since the difference in flow curves measured at RT and 50 °C is not significant for DP780, the springback predictions shown in Fig. 12 are not likely to be affected by temperature.

The same analysis was done for TRIP780 steel sheet. For the pre-strained material, the flow stress is assumed to be close to the segment A_2–B_2 in Fig. 17(b) during forming stage because the transformation is almost completed during the first

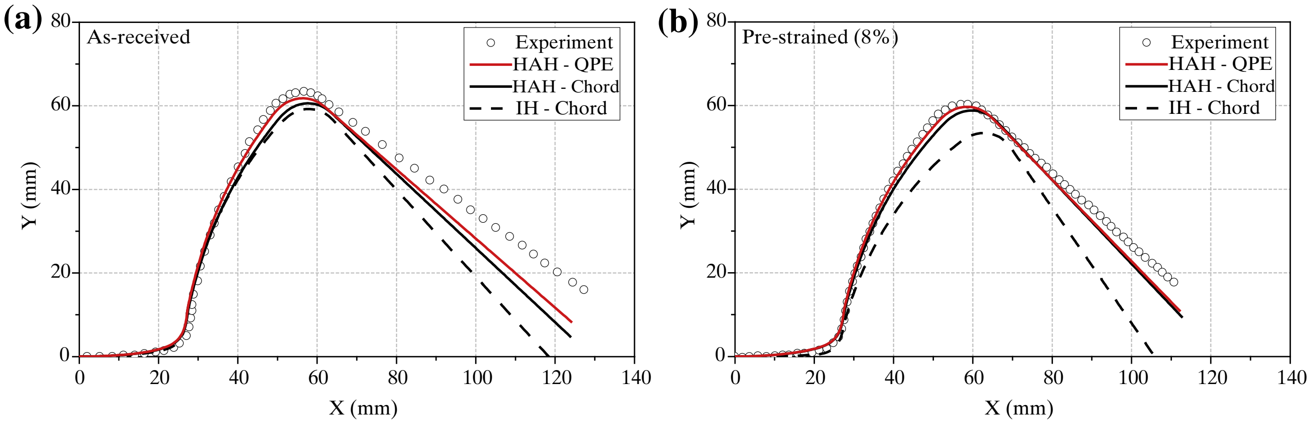

Fig. 12. Springback profile of DP780 steel sheet for (a) as-received specimen and (b) pre-strained specimen.

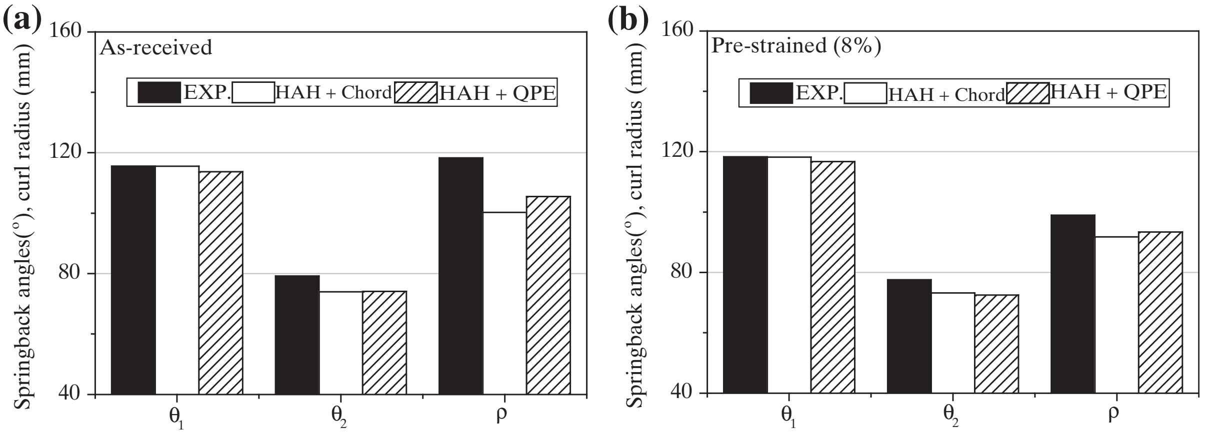

Fig. 13. Springback parameters of DP780 steel sheet for (a) as-received specimen and (b) pre-strained specimen.

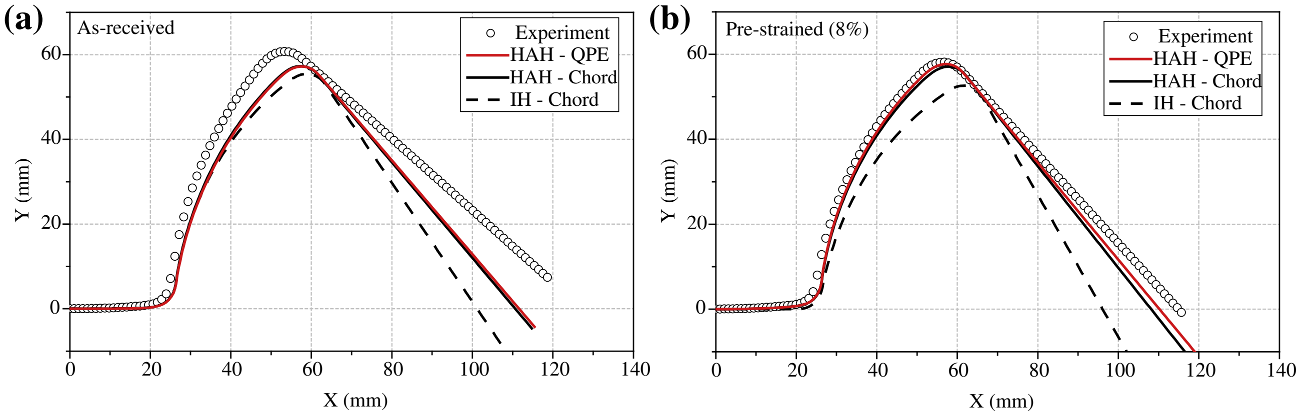

Fig. 14. Springback profile of TRIP780 steel sheet for (a) as-received specimen and (b) pre-strained specimen.

tensile loading. Then, temperature is not a critical factor for springback prediction like for DP780. However, for the as-received material the flow stress can be close to the segment $O–B_1$ in Fig. 17(b) during forming. Because the flow curves of TRIP780 measured at RT and 50 °C are significantly different, temperature, which is not taken into account in the predictions shown in Fig. 14(a), is likely to influence springback.

Fig. 18 shows the springback predictions for the as-received TRIP780 steel sheet considering the temperature effect. The same HAH and QPE parameters were used excepted for the isotropic hardening curve, which was that measured at 50 °C for

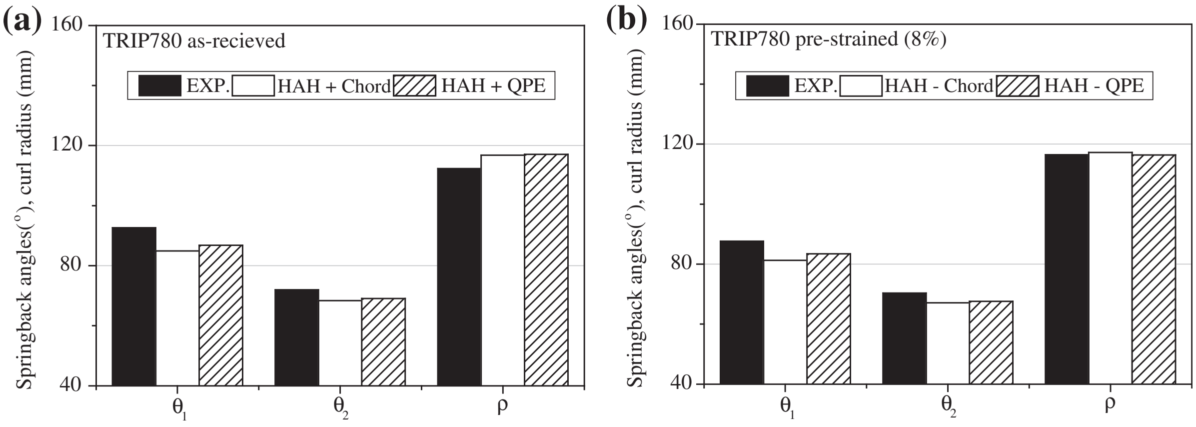

Fig. 15. Springback parameters of TRIP780 steel sheet for (a) as-received specimen and (b) pre-strained specimen.

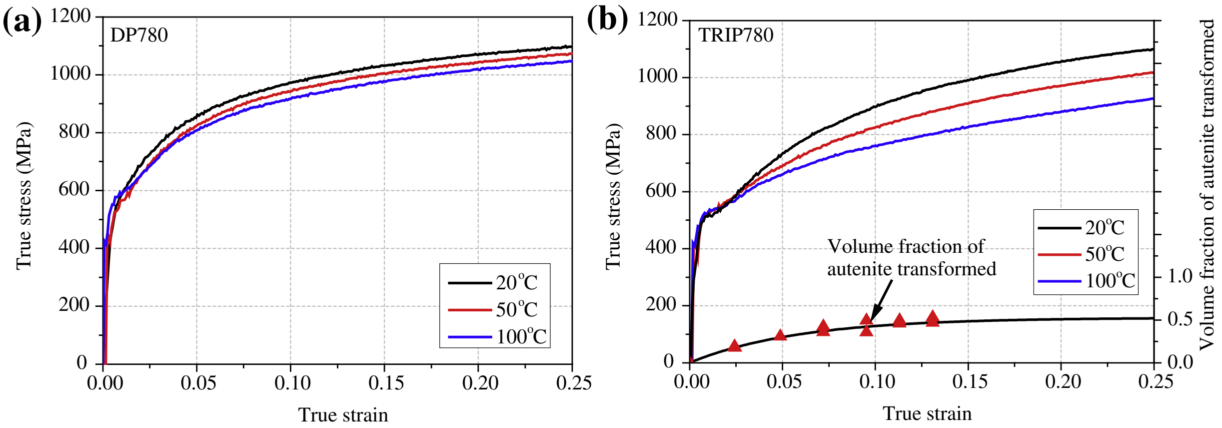

Fig. 16. Bulge stress–strain curves at different temperatures for (a) DP780 and (b) TRIP780 steel sheets. The volume fraction of transformed austenite is only for the room temperature.

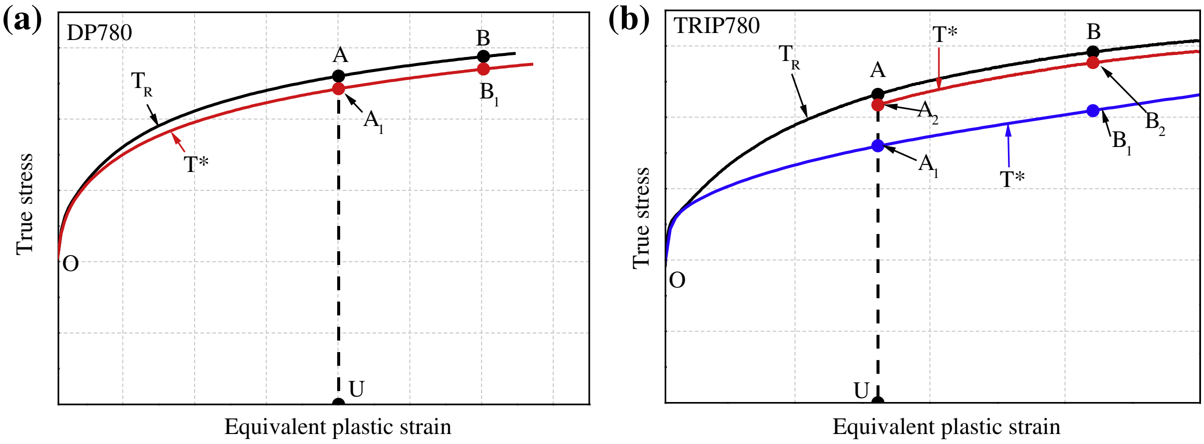

Fig. 17. Schematic illustrations of stress–strain response during forming stage in U-draw bending for (a) DP780, (b) TRIP780 steel sheets($TR < T^*$).

TRIP780 steel in Fig. 16(b). Fig. 18 shows that the temperature effect leads to a better prediction of springback. The residual between predicted and experimental springback is likely due to friction effect. For a thorough investigation using thermo-mechanical simulations, forward–reverse loading experiments at different temperatures are necessary (Piao et al., 2012).

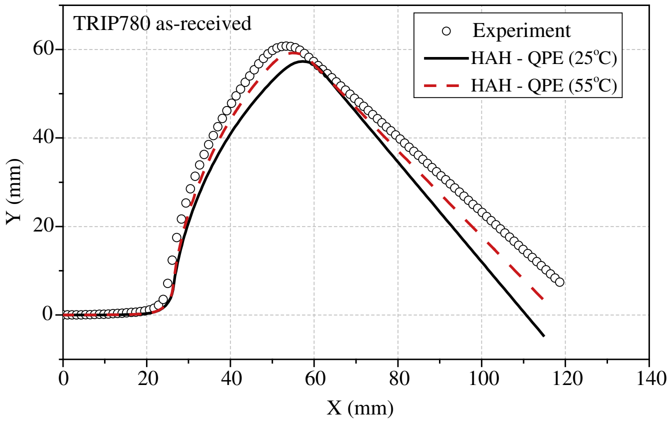

Fig. 18. Springback profiles predicted with different plastic hardening curves.

6. Conclusions

In this work, the quasi-plastic–elastic (QPE) model was extended and combined with the homogeneous anisotropic hardening model (HAH). The corresponding fully implicit numerical algorithm for plane stress condition was proposed. By combining the two modeling approaches, the Bauschinger effect, transient behavior, permanent softening and plasticity-induced elastic modulus degradation could be accurately simulated. Moreover, the stress integration algorithm for the coupled elastic–plastic modeling approach could be applied with a general non-quadratic anisotropic yield function. Accounting for the nonlinear elastic unloading/reloading behavior and the complex plastic flow stress upon load reversal with QPE and HAH models, respectively, enhanced accuracy in springback predictions.

The material parameters for the advanced material models were obtained by the Nelder–Mead simplex algorithm. Finite element simulations using simple boundary conditions were carried out for DP780 and TRIP780 steel sheets. These simulations validated the proposed HAH–QPE approach and its numerical implementation by reproducing a few stress–strain curves cycles for both materials. In particular, the QPE approach could well capture the nonlinear unloading behavior compared with the frequently used linear "Chord" type approach.

Finally, finite element simulations of U-draw/bending were carried out for the springback prediction for as-received specimen and pre-deformed AHSS sheets deformation. It was found that the prediction of springback was improved when the advanced models for both plastic flow stress and elastic unloading were taken into account.

Although the present FE simulations using the combined HAH–QPE model resulted in good predictions for most of the cases, the springback of TRIP780 steel sheet with as-received specimen was initially overestimated. This significant discrepancy between simulation and experiment for the TRIP780 steel sheet was analyzed by introducing the temperature effect on the phase transformation from austenite to martensite. The measured stress–strain curve at different temperatures and the transformed volume fraction of retained austenite could provide reasonably good explanation on the reason of the discrepancy.

Acknowledgments

This research was supported by POSCO. K. Chung appreciates the support by the National Research Foundation of Korea Grant funded by the Korean Government (NRF-2010-220-D00037. Myoung-Gyu Lee appreciates the support by the grants from the Industrial Source Technology Development Program (#10040078) of MKE and from the ERC program of National Research Foundation of Korea (NRF-2012R1A5A1048294).

References

ABAQUS, 2010. User's Manual (Version 6.10). Hibbit, Karlsson & Sorensen Inc, USA.

Andar, M.O., Kuwabara, T., Yonemura, S., Uenishi, A., 2010. Elastic–plastic and inelastic characteristics of high strength steel sheets under biaxial loading and unloading. ISIJ International 50, 613–619.

Aretz, H., 2008. A simple isotropic-distortional hardening model and its application in elastic–plastic analysis of localized necking in orthotropic sheet metals. International Journal of Plasticity 24, 1457–1480.

Armstrong, P.J., Frederick, C.O. 1966. A Mathematical representation of the multiaxial Bauschinger effect, Central Electricity Generating Board Report. Berkeley Nuclear Laboratories.

Barlat, F., Brem, J.C., Yoon, J.W., Chung, K., Dick, R.E., Lege, D.J., Pourboghrat, F., Choi, S.H., Chu, E., 2003. Plane stress yield function for aluminum alloy sheets – Part 1: Theory. International Journal of Plasticity 19, 1297–1319.

Barlat, F., Gracio, J.J., Lee, M.G., Rauch, E.F., Vincze, G., 2011. An alternative to kinematic hardening in classical plasticity. International Journal of Plasticity 27, 1309–1327.

Barlat, F., Ha, J., Grácio, J.J., Lee, M.-G., Rauch, E.F., Vincze, G., 2012. Extension of homogeneous anisotropic hardening model to cross-loading with latent effects. International Journal of Plasticity. http://dx.doi.org/10.1016/j.ijplas.2012.07.002.

Cardoso, R.P.R., Yoon, J.W., 2009. Stress integration method for a nonlinear kinematic/isotropic hardening model and its characterization based on polycrystal plasticity. International Journal of Plasticity 25, 1684–1710.

Chaboche, J.L., 1986. Time-independent constitutive theories for cyclic plasticity. International Journal of Plasticity 2, 149–188.

Chatti, S., Hermi, N., 2011. The effect of non-linear recovery on springback prediction. Computers and Structures 89, 1367–1377.

Choi, Y., Han, C.-S., Lee, J.K., Wagoner, R.H., 2006a. Modeling multi-axial deformation of planar anisotropic elasto-plastic materials, Part I: Theory. International Journal of Plasticity 22, 1745–1764.

Choi, Y., Han, C.-S., Lee, J.K., Wagoner, R.H., 2006b. Modeling multi-axial deformation of planar anisotropic elasto-plastic materials, Part II: Applications. International Journal of Plasticity 22, 1765–1783.

Chung, K., Lee, M.G., Kim, D., Kim, C., Wenner, M.L., Barlat, F., 2005. Spring-back evaluation of automotive sheets based on isotropic–kinematic hardening laws and non-quadratic anisotropic yield functions: Part I: Theory and formulation. International Journal of Plasticity 21, 861–882.

Cleveland, R.M., Ghosh, A.K., 2002. Inelastic effects on springback in metals. International Journal of Plasticity 18, 769–785.

Dafalias, Y.F., Popov, E.P., 1976. Plastic internal variables formalism of cyclic plasticity. Journal of Applied Mechanics Series E 43, 645–651.

Darendeliler, H., Akkök, M., Yücesoy, C.A., 2002. Effect of variable friction coefficient on sheet metal drawing. Tribology International 35, 97–104.

De Borst, R., Feenstra, P.H., 1990. Studies in anisotropic plasticity with reference to the hill criterion. International Journal for Numerical Methods in Engineering 29, 315–336.

Dutko, M., Perić, D., Owen, D.R.J., 1993. Universal anisotropic yield criterion based on superquadric functional representation: Part 1. Algorithmic issues and accuracy analysis. Computer Methods in Applied Mechanics and Engineering 109, 73–93.

Eggertsen, P.A., Mattiasson, K., 2010. On constitutive modeling for springback analysis. International Journal of Mechanical Sciences 52, 804–818.

Fei, D., Hodgson, P., 2006. Experimental and numerical studies of springback in air v-bending process for cold rolled TRIP steels. Nuclear Engineering and Design 236, 1847–1851.

Feigenbaum, H.P., Dafalias, Y.F., 2007. Directional distortional hardening in metal plasticity within thermodynamics. International Journal of Solids and Structures 44, 7526–7542.

Feigenbaum, H.P., Dafalias, Y.F., 2008. Simple model for directional distortional hardening in metal plasticity within thermodynamics. Journal of Engineering Mechanics 134, 730–738.

François, M., 2001. A plasticity model with yield surface distortion for non proportional loading. International Journal of Plasticity 17, 703–717.

Geng, L., Shen, Y., Wagoner, R.H., 2002. Anisotropic hardening equations derived from reverse-bend testing. International Journal of Plasticity 18, 743–767.

Geng, L., Wagoner, R.H., 2002. Role of plastic anisotropy and its evolution on springback. International Journal of Mechanical Sciences 44, 123–148.

Ha, J.-J., 2012. Evaluation of Constitutive Models for Non-Proportional Deformation. Graduate Institute of Ferrous Technology, Pohang University of Science and Technology.

Hill, R., Hecker, S.S., Stout, M.G., 1994. An investigation of plastic flow and differential work hardening in orthotropic brass tubes under fluid pressure and axial load. International Journal of Solids and Structures 31, 2999–3021.

Kim, H., Altan, T., Yan, Q., 2009. Evaluation of stamping lubricants in forming advanced high strength steels (AHSS) using deep drawing and ironing tests. Journal of Materials Processing Technology 209, 4122–4133.

Kurtyka, T., Życzkowski, M., 1996. Evolution equations for distortional plastic hardening. International Journal of Plasticity 12, 191–213.

Lee, J.-W., Lee, M.-G., Barlat, F., 2012a. Finite element modeling using homogeneous anisotropic hardening and application to spring-back prediction. International Journal of Plasticity 29, 13–41.

Lee, J.-Y., Lee, J.-W., Lee, M.-G., Barlat, F., 2012b. An application of homogeneous anisotropic hardening to springback prediction in pre-strained U-draw/bending. International Journal of Solids and Structures. http://dx.doi.org/10.1016/j.ijsolstr.2012.03.042.

Lee, J., Lee, M.-G., Barlat, F., Kim, J.H., 2012c. Stress integration schemes for novel homogeneous anisotropic hardening model. Computer Methods in Applied Mechanics and Engineering 247–248, 73–92.

Lee, M.-G., Kim, S.-J., Han, H.N., 2010. Crystal plasticity finite element modeling of mechanically induced martensitic transformation (MIMT) in metastable austenite. International Journal of Plasticity 26, 688–710.

Lee, M.G., Kim, C., Pavlina, E.J., Barlat, F., 2011. Advances in sheet forming-materials modeling numerical simulation and press technologies. Journal of Manufacturing Science and Engineering, Transactions of the ASME 133.

Lee, M.G., Kim, D., Kim, C., Wenner, M.L., Chung, K., 2005a. Spring-back evaluation of automotive sheets based on isotropic–kinematic hardening laws and non-quadratic anisotropic yield functions, Part III: Applications. International Journal of Plasticity 21, 915–953.

Lee, M.G., Kim, D., Kim, C., Wenner, M.L., Wagoner, R.H., Chung, K., 2005b. Spring-back evaluation of automotive sheets based on isotropic–kinematic hardening laws and non-quadratic anisotropic yield functions: Part II: Characterization of material properties. International Journal of Plasticity 21, 883–914.

Lee, M.G., Kim, D., Kim, C., Wenner, M.L., Wagoner, R.H., Chung, K., 2007. A practical two-surface plasticity model and its application to spring-back prediction. International Journal of Plasticity 23, 1189–1212.

Li, K.P., Carden, W.P., Wagoner, R.H., 2002. Simulation of springback. International Journal of Mechanical Sciences 44, 103–122.

Matuszak, A., 2000. Factors influencing friction in steel sheet forming. Journal of Materials Processing Technology 106, 250–253.

Morestin, F., Boivin, M., 1996. On the necessity of taking into account the variation in the Young modulus with plastic strain in elastic–plastic software. Nuclear Engineering and Design 162, 107–116.

Nelder, J.A., Mead, R., 1965. A Simplex method for function minimization. The Computer Journal 7, 308–313.

NUMISHEET, 1993. NUMISHEET'93 Benchmark Problem. In: Makinouchi, A., Nakamachi,E., Onate E., Wagoner, R.H. (Ed.), Proceedings of 2nd International Conference on Numerical Simulation of 3D Sheet Metal Forming Processes-Verification of Simulation with Experiment, Isehara, Japan.

NUMISHEET, 2011. NUMISHEET 2011 Benchmark. In: Chung, K., Huh, H., Han, H.-N., Moon, Y.H., Barlat, F. (Ed.), The 8th International Conference and Workshop on Numerical Simulation of 3D Sheet Metal Forming Processes, Seoul, Korea.

Oliveira, M.C., Alves, J.L., Chaparro, B.M., Menezes, L.F., 2007. Study on the influence of work-hardening modeling in springback prediction. International Journal of Plasticity 23, 516–543.

Ortiz, M., Simo, J.C., 1986. Analysis of a new class of integration algorithms for elastoplastic constitutive relations. International Journal for Numerical Methods in Engineering 23, 353–366.

Park, M.S., Lee, B.C., 1996. Geometrically non-linear and elstoplastic three-dimensional shear flexible beam element of von-Mises-type hardening material. International Journal for Numerical Methods in Engineering 39, 383–408.

Piao, K., Lee, J.K., Kim, J.H., Kim, H.Y., Chung, K., Barlat, F., Wagoner, R.H., 2012. A sheet tension/compression test for elevated temperature. International Journal of Plasticity. http://dx.doi.org/10.1016/j.ijplas.2012.03.009.

Prager, W., 1956. A new method of analyzing stresses and strains in work hardening plastic solids. Journal of Applied Mechanics 23, 493–496.

Simo, J.C., Hughes, T.J.R., 1998. Computational Inelasticity. Springer-Verlag.

Sun, L., Wagoner, R.H., 2011. Complex unloading behavior: nature of the deformation and its consistent constitutive representation. International Journal of Plasticity 27, 1126–1144.

Sung, J.H., Kim, J.H., Wagoner, R.H., 2010. A plastic constitutive equation incorporating strain, strain-rate, and temperature. International Journal of Plasticity 26, 1746–1771.

Tugcu, P., Neale, K.W., 1999. On the implementation of anisotropic yield functions into finite strain problems of sheet metal forming. International Journal of Plasticity 15, 1021–1040.

Vincent, L., Calloch, S., Kurtyka, T., Marquis, D., 2002. An improvement of multiaxial ratchetting modeling via yield surface distortion. Journal of Engineering Materials and Technology 124, 402–411.

Voyiadjis, G.Z., Foroozesh, M., 1990. Anisotropic distortional yield model. Journal of Applied Mechanics 57, 537–547.

Wu, H.-C., 2002. Anisotropic plasticity for sheet metals using the concept of combined isotropic–kinematic hardening. International Journal of Plasticity 18, 1661–1682.

Wu, H.-C., 2003. On finite plastic deformation of anisotropic metallic materials. International Journal of Plasticity 19, 91–119.

Wu, H.-C., 2007. On stress rate and plasticity constitutive equations referred to a body-fixed coordinate system. International Journal of Plasticity 23, 1486–1511.

Yamaguchi, K., Adachi, H., Takakura, N., 1998. Effects of plastic strain and strain path on Young's modulus of sheet metals. Metals and Materials International 4, 420–425.

Yang, M., Akiyama, Y., Sasaki, T., 2004. Evaluation of change in material properties due to plastic deformation. Journal of Materials Processing Technology 151, 232–236.

Yoon, J.W., Yang, D.Y., Chung, K., 1999a. Elasto-plastic finite element method based on incremental deformation theory and continuum based shell elements for planar anisotropic sheet materials. Computer Methods in Applied Mechanics and Engineering 174, 23–56.

Yoon, J.W., Yang, D.Y., Chung, K., Barlat, F., 1999b. A general elasto-plastic finite element formulation based on incremental deformation theory for planar anisotropy and its application to sheet metal forming. International Journal of Plasticity 15, 35–67.

Yoshida, F., Uemori, T., 2002. A model of large-strain cyclic plasticity describing the Bauschinger effect and work hardening stagnation. International Journal of Plasticity 18, 661–686.

Yoshida, F., Uemori, T., Fujiwara, K., 2002. Elastic–plastic behavior of steel sheets under in-plane cyclic tension–compression at large strain. International Journal of Plasticity 18, 633–659.

Yu, H.Y., 2009. Variation of elastic modulus during plastic deformation and its influence on springback. Materials and Design 30, 846–850.

Zang, S.L., Liang, J., Guo, C., 2007. A constitutive model for spring-back prediction in which the change of Young's modulus with plastic deformation is considered. International Journal of Machine Tools and Manufacture 47, 1791–1797.

Ziegler, H., 1959. A modification of Prager's hardening rule. Quarterly of Applied Mathematics 17, 55–65.